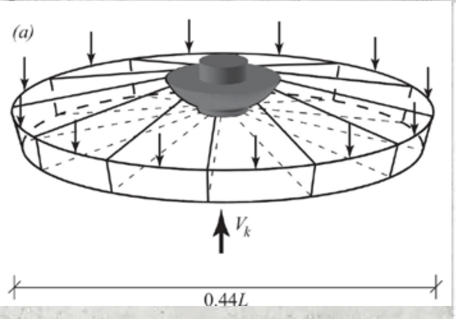

Seismic behaviour of flat slabs

Ecole Polytechnique Fédérale de Lausanne
Institut d'Ingénierie Civile
Laboratoire de Construction en Béton

Prof. Dr. Aurelio Muttoni
Prof. Dr. Katrin Beyer
Ioannis-Sokratis Drakatos

cemsuisse-Projekt 201201 – Oktober 2015
Diese Forschungsarbeit wurde durch cemsuisse, Verband
der Schweizerischen Cementindustrie mitfinanziert

Vorwort

Das Forschungsprojekt „Erdbebenverhalten von Flachdecken“ hatte zum Ziel zu beurteilen, inwiefern Gebäude mit Flachdecken in der Schweiz erdbebengefährdet sind. Dazu wurden Modelle und Methoden entwickelt werden, die es dem Ingenieur erlauben, die Momenten- und Rotationskapazität von Flachdecken unter Erdbebeneinwirkung zu bestimmen. Das Forschungsprojekt „Erdbebenverhalten von Flachdecken“ wollte beurteilen, inwiefern Gebäude mit Flachdecken in der Schweiz erdbebengefährdet sind. Dazu wurden Modelle und Methoden entwickelt werden, die es dem Ingenieur erlauben, die Momenten- und Rotationskapazität von Flachdecken unter Erdbebeneinwirkung zu bestimmen. Die Ergebnisse zeigen, dass für mittelhohe, im Grund- und Aufriss regelmässige Gebäude, die durch Stahlbetonwände ausgesteift sind, die Tragsicherheit der Flachdecken unter der geringen bis mittleren Erdbebengefährdung der Schweiz häufig nicht kritisch ist.

Die cemsuisse Forschungsförderung unterstützt Forschungsprojekte im Bereich der Betonanwendung, welche von kompetenten Forschergruppen an cemsuisse herangetragen werden. Mit der proaktiven Forschungsförderung definiert cemsuisse zudem Forschungsprojekte von Interesse und trägt diese an kompetente Forschergruppen heran oder schreibt sie öffentlich aus. Die Projektnehmer werden jeweils von einer Begleitgruppe aus cemsuisse – Vertretern fachlich unterstützt.

Dr. Heiner Widmer, Leiter Umwelt, Technik, Wissenschaft, cemsuisse

SEISMIC BEHAVIOUR OF FLAT SLABS

CEMSUISSE PROJECT 201201

FINAL REPORT

Prof. Dr. Aurelio Muttoni
Prof. Dr. Katrin Beyer
Ioannis-Sokratis Drakatos

Structural Concrete Laboratory

Earthquake Engineering and Structural Dynamics Laboratory

École Polytechnique Fédérale de Lausanne
Lausanne, October 2015

Notations

Latin upper case letters

B	specimen size
M_{exp}	observed maximum moment introduced to the slab-column connection
M_{pred}	predicted maximum moment introduced to the slab-column connection
M_{peak}	maximum moment introduced to the slab-column connection
N	number of applied cycles
V_{test}	shear force applied to the slab specimen
V_{peak}	peak shear force applied to the slab specimen (e= cst)
V_R	shear force transferred from the slab to the column at failure

Latin lower case letters

b_o	control perimeter (located at a distance $d/2$ from the column faces)
c	column size
d	average effective depth
d_g	maximum aggregate size
f_c'	concrete compressive strength
f_y	yield stress of reinforcing bar
h	slab thickness

Greek upper case letters

Δ_{max}	maximum slab deflection due to vertical and lateral loads
Δ_{min}	maximum slab deflection due to vertical and lateral loads
$\Delta_{V.max}$	maximum slab deflection due to vertical loads
Δ_{V+L}	slab deflection due to vertical and lateral loads

Greek lower case letters

ρ	top flexural reinforcement ratio
ρ'	bottom flexural reinforcement ratio
ψ_{max}	maximum local slab rotation
$\psi_{max.p}$	maximum local slab rotation at maximum moment
ψ_{min}	minimum local slab rotation
ψ_{st}	interstory drift rotation
ψ_{col}	drift rotation due to column deformation
ψ_{scc}	connection rotation
$\psi_{scc.exp}$	observed connection rotation at maximum moment
$\psi_{scc.peak}$	connection rotation at maximum moment
$\psi_{scc.pred}$	predicted connection rotation at maximum moment

1 Introduction

1.1 Context

The structural system of flat slabs is widely used in Swiss and international building construction as it offers significant advantages for all involved stakeholders (owners, engineers, architects, and constructors). Beamless floor systems present an elegant structural solution offering large open spaces and versatility in terms of space division, advantages that are particularly appreciated for office buildings. In addition, the absence of beams allows for a reduced story height. Moreover, the simplified formwork offers the advantage of reduced construction time, rendering the construction of flat slabs a cost-effective solution. The aforementioned advantages are counterbalanced by the significant slab self-weight with regard to other floor systems such as reinforced concrete beam-slab systems, concrete-steel mixed systems or timber systems. Moreover, since the behaviour of slab-column connections can be very brittle, signs of incoming failure cannot be easily detected in advance.

For any earthquake-resistant design, increased floor weight and brittle behaviour of members should be avoided and as a result the structural system of flat slabs is not commonly used in seismic prone areas. Nevertheless, the exclusion of slab-column connections from the lateral force-resisting system as well as the use of transverse reinforcement—which enhances the connection ductility—have led to significant rise in popularity of flat slabs in several regions under moderate to high seismicity (e.g. in California). However, post-earthquake observations have shown that slab-column connections designed to carry only gravity loads can be susceptible to brittle punching failure due to deformations imposed by the members that provide lateral resistance and stiffness to the building such as core walls around elevator shafts and staircases or shear walls. In addition, research on the seismic behaviour of slab-column connections (carried out mostly by researchers in North America) has shown that slabs without transverse reinforcement can be vulnerable to earthquake loading.

Although the design of this structural system against permanent loads is a rather conventional procedure for the structural engineer, designing buildings with slab-column connections to sustain lateral displacements due to seismic excitation, even if they do not belong to the lateral force-resisting system, is less straightforward, since the complex three-dimensional behavior of slab-column connections under displacement-induced moments is not yet completely understood. As a result, the codes of practice provide empirical design formulas based on experimental evidence rather than mechanical models for the seismic design of slab-column connections.

1.2 Research objectives

The presented research aims to assess the seismic vulnerability of Swiss buildings with flat slabs and to provide to Swiss engineers tools for the design and assessment of flat slabs considering the deformations imposed by earthquakes. This research project was performed simultaneously with an experimental research project funded by the Swiss National Science Foundation (Grant 143747).

1.3 Report objectives and organization

The present report focuses on the engineering models that have been developed for assessing the seismic demand on slab-column connections and their corresponding capacity. In addition it provides an overview of the performed work, as well as the obtained results of the research project. The report is organized as follows: a brief presentation of the state of the art is followed by the presentation of a physical model for the moment-rotation relationship of slab-column connections and its validation using experiments found in the literature. Afterwards, on the basis of the proposed model, a numerical analysis method for the calculation of the seismic moment demands in slab-column connections is presented. The vulnerability classification of Swiss buildings with slab-column connections is performed in the last part of this report, combining the content of the previous two parts.

2. State of the art

2.1 Swiss code SIA 262/2013

For the design of slab-column connections against vertical loads, the Swiss code SIA 262 [10] is based on the Critical Shear Crack Theory [6], developed at EPFL, since it has shown very good agreement with experimental results. Although currently there is no provision for the seismic design of slab-column connections, the Critical Shear Crack Theory can be extended for the cases of seismically-induced deformations since it considers both load and deformation of the slab.

2.2 ACI 318-2014

For the seismic design of slab-column connections, the ACI 318-14 [1] adopts a simplified eccentric shear transfer model for the moment resistance. The interstory drift capacity of slab-column connections is given by an empirical relationship as a function of the vertical load acting on the slab-column connection.

3. Physical model for punching resistance under seismic loading

3.1 Assumptions

This section presents the theoretical background of the proposed model for the moment-rotation relationship of a slab-column connection subjected to a seismically-induced moment. The model is derived from the axisymmetric model developed by Kinnunen & Nylander [5] and Muttoni [6] for slabs subjected to gravity loads. In the original model, the slab is divided into an even number n of sector elements and the region inside the shear crack (Figure 2a). Since that model is axisymmetric, the equilibrium formulation can be reduced to one sector element (Figure 2a).

For the case of seismically-induced moment, several modifications of the axisymmetric analytical model are introduced. Finite element analyses (Figure 1a) and tests on slab-column connections subjected to constant shear force and increasing moment [4] showed that the slab rotation at different angles follows approximately a sinusoidal law, as described by the following expression:

$$\psi(\varphi)=\frac{\psi_{max}+\psi_{min}}{2}+\frac{\psi_{max}-\psi_{min}}{2}\cdot sin(\varphi) \tag{1}$$

where φ is the angle in regards to the direction of seismic loading and ψ_{max} and ψ_{min} are the maximum slab rotation for $\varphi = \pi/2$ and the minimum slab rotation for $\varphi = 3\pi/2$, respectively (Figure 1a).

Moreover, finite element analyses (Figure 1b) and experimental evidence show that radial curvature concentrates in the column area which is located inside the shear cracks [6]. In case of slab-column connections with unbalanced moment M, tests by Drakatos et al. [4] show that the inclination of critical shear cracks depends on the ratio of unbalanced moment M to the shear force V, subsequently referred to as eccentricity e. Based on these observations, it is assumed that the radius r_0 of the critical shear crack is equal to $e = M / V$, but not smaller than $r_c + d$ as assumed by [6]:

$$r_0=e\geq r_c+d \tag{2}$$

where r_c is the radius of the column and d is the slab effective depth.

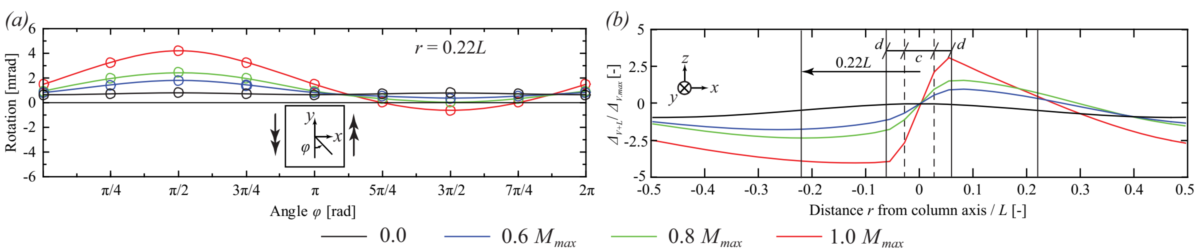

Figure 1: (a) Local slab rotations at varying angles and (b) slab deflections parallel to the x-axis for different lateral load levels according to finite element analysis.

3.2 Moment-rotation relationship

- *Equilibrium of sector elements (local level)*

The kinematic assumption of the proposed model is shown in Figure 2a. Figure 2b illustrates the curvature distribution along the x axis (see Figure 1a) for the case of negligible shear force compared to the unbalanced moment for both slab halves subjected to hogging and sagging bending moments due to seismic loading, subsequently referred to as hogging and sagging slab halves, respectively. Figure 3 shows the free body diagram for the sector element at angle φ_i and the slab portion inside the shear crack. As a result of varying slab rotations at different angles φ in addition to the moment due to flexure, a moment due to torsion and eccentric shear force is also introduced to the slab-column connection.

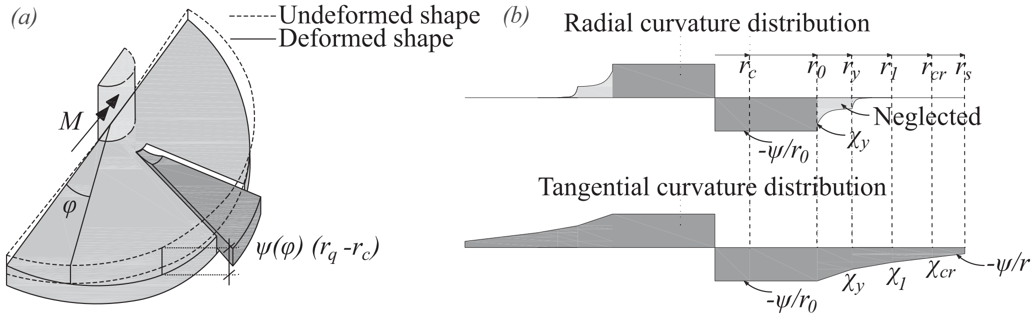

Figure 2: Proposed mechanical model: (a) kinematic assumption for the rotations of the sector elements (hogging slab half), and (b) distribution of radial and tangential curvatures along the diameter of the isolated slab element (when gravity load induced moment are neglected).

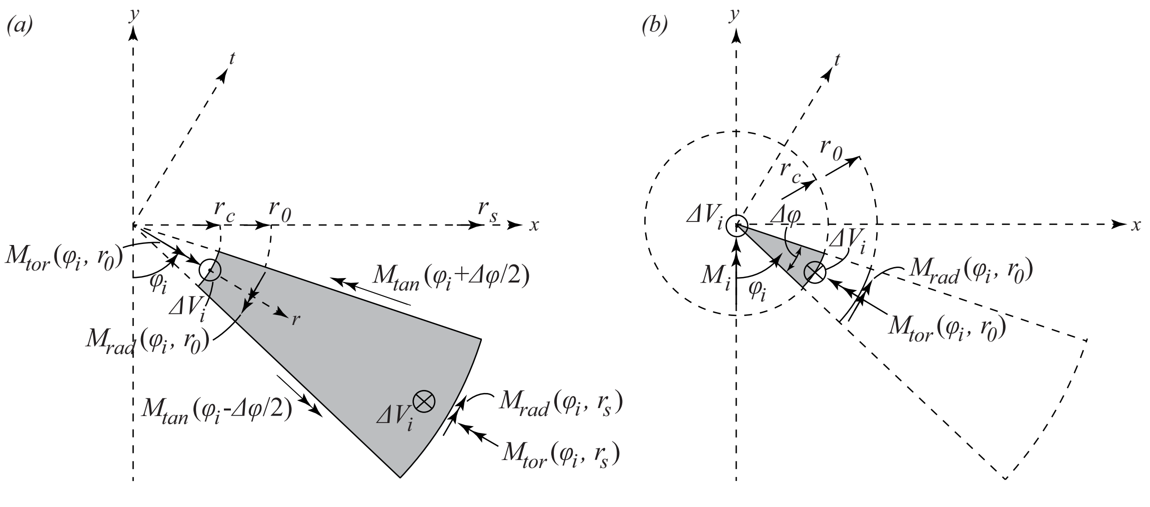

Figure 3: Internal forces acting on the slab region (hogging slab half): (a) outside the shear crack, and (b) inside the shear crack.

$M_{tan}(\varphi_i\text{-}\Delta\varphi/2)$ and $M_{tan}(\varphi_i+\Delta\varphi/2)$ are the integrals of the tangential moments at the faces of each sector element (Figure 3a). These moments can be determined directly as a function of the assumed rotation and a quadri-linear moment-curvature relationship [6]:

$$M_{tan}(\varphi)=\begin{pmatrix} m_R\cdot\langle r_y-r_0\rangle+EI_1\cdot\psi(\varphi)\cdot\langle ln(r_1)-ln(r_y)\rangle+EI_1\cdot\chi_{TS}\cdot\langle r_1-r_y\rangle+ \\ m_{cr}\cdot\langle r_{cr}-r_1\rangle+EI_0\cdot\psi(\varphi)\cdot\langle ln(r_s)-ln(r_{cr})\rangle \end{pmatrix} \tag{3}$$

where EI_0 and EI_1 are the slab stiffness before and after cracking, m_{cr} and m_R are the cracking moment and moment capacity, respectively, per unit width, χ_{TS} is the curvature due to the tension stiffening effect, and r_0, r_y, r_1, r_{cr} and r_s are the radii of the critical shear crack, of the yielded zone, of the zone in which cracking is stabilized, of the cracked zone and of the circular isolated slab element, respectively. The operator $\langle x\rangle$ is x for $x \geq 0$ and 0 for $x < 0$. Eq.

(3) for the calculation of the tangential moment $M_{tan}(\varphi)$ is taken directly from the analytical model proposed by Muttoni [6]. For the case of seismically-induced deformations the local slab rotation ψ is dependent on the angle φ of the sector element with regard to the direction of seismic loading and the radius r_0 of the critical shear crack is updated as a function of the eccentricity (see Eq. (2)) to take into account the fact that the shear force becomes less determinant as eccentricity increases. Therefore, the integral of the radial moment for a sector element at angle φ at $r = r_0$ is:

$$M_{rad}(\varphi, r_0)=m_r(\varphi)\cdot r_0\cdot\Delta\varphi \tag{4}$$

where $m_r(\varphi)$ is the radial moment per unit width at $r = r_0$ as function of the radial curvature [6].

If φ_i is the angle formed by the axis of bending and the bisector of the i^{th} sector element, the shear force that can be carried by this sector element is derived by moment equilibrium in the tangential direction with respect to the center of the column with radius r_c:

$$\Delta V_i\cdot=\frac{1}{r_q-r_c}\left\{M_{rad}\left(\varphi_i, r_0\right) - M_{rad}\left(\varphi_i, r_s\right)+\left[M_{tan}\left(\varphi_i+\frac{\Delta\varphi}{2}\right)+M_{tan}\left(\varphi_i-\frac{\Delta\varphi}{2}\right)\right]\cdot\sin\left(\frac{\Delta\varphi}{2}\right)\right\} \tag{5}$$

The moment equilibrium in the radial direction gives the torsional moment that is carried by the connection for the i^{th} sector element:

$$M_{tor}(\varphi_i, r_0)=\left[M_{tan}\left(\varphi_i+\frac{\Delta\varphi}{2}\right)-M_{tan}\left(\varphi_i-\frac{\Delta\varphi}{2}\right)\right]\cdot\cos\left(\frac{\Delta\varphi}{2}\right)+M_{tor}(\varphi_i, r_s) \tag{6}$$

The radial and torsional moments at the perimeter of each sector element $M_{rad}(\varphi_i, r_s)$ and $M_{tor}(\varphi_i, r_s)$ (Eq. (5) and (6), respectively) are obtained using the Effective Beam Width Method, as will be shown in the following section.

Equilibrium of shear forces at the column edge gives the total shear force acting on the connection for the load step k:

$$V_k=\sum_{i=1}^{n}\Delta V_i \tag{7}$$

Moment equilibrium at the column edge gives the total moment acting on the connection (parallel to the transferred moment) for the load step k:

$$M_k=\sum_{i=1}^{n}M_{rad}\left(\varphi_i, r_0\right)\cdot\sin(\varphi_i)+\sum_{i=1}^{n}M_{tor}(\varphi_i, r_0)\cdot\cos(\varphi_i)+\sum_{i=1}^{n}\Delta V_i\cdot r_c\cdot\sin(\varphi_i) \tag{8}$$

The three terms of Eq. 8 represent the contribution of flexure, torsion and eccentric shear force to the total unbalanced moment.

- *Equilibrium of slab specimen (global level)*

For the case of uniformly distributed vertical loading alone, formulating the equilibrium for one sector element is equivalent to formulating the equilibrium for the entire circular slab since $\psi_{max} = \psi_{min} = \psi_v$ (Figure 4a). If a seismic moment is added, the slab rotations vary between sector elements and therefore equilibrium has to be formulated locally for each sector element and globally for the entire circular slab (Figure 4b).

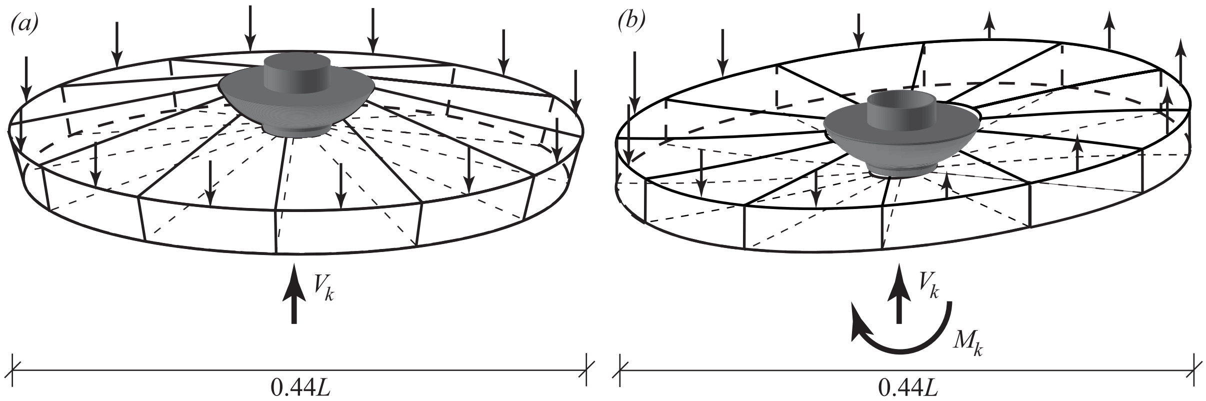

Figure 4: Assumed deformed shape of slab specimen under (a) vertical load [6] and (b) vertical load and imposed lateral deformation.

The unbalanced moment is applied about the *y*-axis. The adoption of the kinematic law of Eq. 1 implies symmetry about the *x*-axis ($\varphi = \pi/2$ and $\varphi = 3\pi/2$) and therefore the moment about the *x*-axis is always zero. To ensure global equilibrium about the *y*-axis, the following procedure is adopted: For each load step *k*, a new value of ψ_{max} is chosen. To determine all local slab rotations by means of the sinusoidal law one needs to choose a value ψ_{min} which is iterated such that the sum of all shear forces ΔV_i is equal to the shear force V that is applied to the slab–column connection. The latter is assumed as constant since it results from gravity loads. In order to obtain the moment–rotation curve, the radius r_0 of the shear crack is adapted at each load step *k* as it is assumed to be equal to the attained eccentricity:

$$e_k = M_k / V_k \tag{9}$$

The aforementioned iterative procedure can also be used if M_k or e_k rather than V_k is constant, situations which can be found when constant horizontal loads act on columns or when slabs with unequal spans are subjected to vertical load alone.

3.3 Relationship between local rotations and interstory drift

For evaluating the seismic performance of buildings in terms of displacements, structural engineers use typically the interstory drift ψ_{st}, i.e., the relative horizontal displacement between two adjacent floors divided by the story height. In structural systems of flat slabs and columns, the deformation of the slab and the column contribute both to the interstory drift:

$$\psi_{st} = \psi_{col} + \psi_{slab} \tag{10}$$

where ψ_{col} and ψ_{slab} are, respectively, the contributions of column deformation and slab deformation to the interstory drift.

In laboratory tests, often only the hogging moment area under gravity loads is represented. It is usually assumed that the limit of this area is located at a distance of $r = 0.22L$ from the column axis, where *L* is the midspan-to-midspan distance. In reality, the slab region inside and outside $r = 0.22L$ are both contributing to the rotation due to slab deformation:

$$\psi_{slab} = \psi_{scc} + \psi_{os} \tag{11}$$

where ψ_{scc} and ψ_{os} are respectively the rotation due to the deformation of the slab column connection (slab region inside $r = 0.22L$) and the rotation due to the deformation of the outer portion of the slab (outside $r = 0.22L$ up to $r = 0.50L$).

- *Slab-column connection rotation (ψ_{scc})*

The previous section yields a relationship between the unbalanced moment M and the local slab rotations $\psi(\varphi)$. To determine a relationship between unbalanced moment and slab-column connection rotation ψ_{scc}, a relationship between the local rotations $\psi(\varphi)$ and the connection rotation ψ_{scc} is needed.

Figure 5a shows the deformed shape of the slab analyzed previously until midspan ($0.50L$). Since the proposed model assumes that only the cone inside the shear crack deforms and each element outside the shear crack behaves as a rigid body, the deformed shape of the top slab surface is linear only outside the shear crack (Figure 4(b)). The connection rotation ψ_{scc} can be defined using either local slab rotations ($\psi_{scc.rot}$) or local slab deflections ($\psi_{scc.defl}$). If the definition is based on rotations, $\psi_{scc.rot}$ can be calculated as the average of the maximum and minimum local rotations ψ_{max} and ψ_{min} (Figure 5a):

$$\psi_{scc.rot} = \frac{\psi_{max} - \psi_{min}}{2} \tag{12}$$

For the deflection definition, the connection rotation $\psi_{scc.defl}$ can be calculated as follows:

$$\psi_{scc.defl} = \frac{\Delta_{max} - \Delta_{min}}{2 \cdot \Delta r + c} \tag{13}$$

where Δ_{max} and Δ_{min} are respectively the maximum and minimum local slab deflections at a distance $\Delta r + c/2 = 0.22L$ from the column axis along x axis (Figure 5a), where c is the column size. The definition of the slab-column connection rotation with respect to test configurations of previous experimental campaigns on isolated specimens is shown in Appendix I.

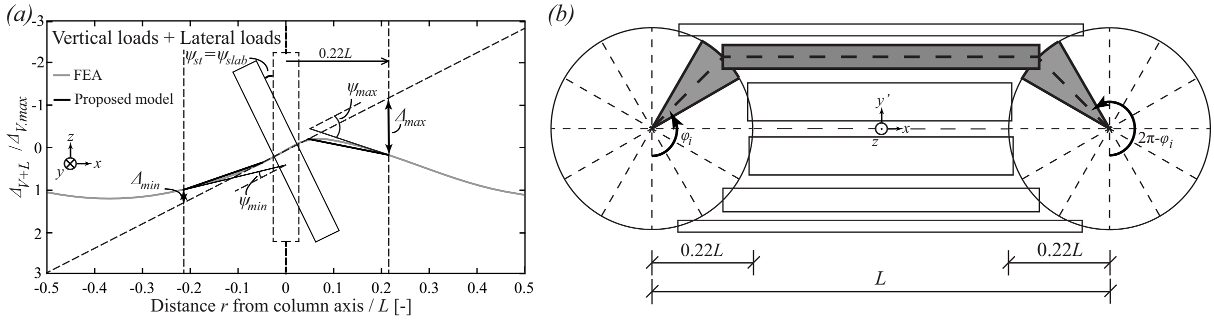

Figure 5: (a) Deformed shape of the slab until midspan according to finite element analysis and the proposed model for combined vertical and lateral loads; and (b) Effective Beam Method for calculating the contribution of the outer slab part to the slab deformation.

- *Rotation due to slab deformation (ψ_{slab})*

The presented model for the moment-rotation relationship considers only the slab region inside $0.22L$ (ψ_{scc}). To obtain an accurate prediction of the total slab deformation ψ_{slab}, the rotation ψ_{os} should also be accounted for. This can be performed by calculating the radial and torsional moments $M_{rad}(\varphi_i, r_s)$ and $M_{tor}(\varphi_i, r_s)$ at the perimeter of each sector element. For this purpose a fixed-fixed beam that connects the perimeter of the considered sector element with the perimeter of the sector element that is symmetric about an axis parallel to the y-axis that passes from the midspan (Figure 5b) is used. When the beam is subjected to a rotation $\psi(\varphi_i)$ at the end of interest and $\psi(2\pi\text{-}\varphi_i)$ at the other end the moment at the end of interest can be found using the elastic solution:

$$M_{y.\,EBW}(\varphi_i)=\frac{2\cdot EI_{k\text{-}1}}{L(\varphi_i)}\left[\psi(\varphi_i)\cdot\sin(\varphi_i)+\frac{\psi_{max}\text{-}\psi_{min}}{2}\cdot\left(2+cos^2(\varphi_i)\cdot\left(1\text{-}3\cdot\frac{r_c}{r_s}\right)\right)\right] \tag{14}$$

where the last term of the multiplication represents the projection of the slab rotation to the y-axis (perpendicular to the axis of each beam), $L(\varphi_i)$ is the length of the beam that connects the sector element at angle φ_i with the sector element at angle $2\pi\text{–}\varphi_i$ and $EI_{k\text{-}1}(\varphi_i)$ is its stiffness calculated using the Effective Beam Width Method:

$$EI_{k\text{-}1}=\frac{M_{k\text{-}1}}{\psi_{slab.k\text{-}1}}\cdot\frac{L(\varphi_i)}{12}\cdot\frac{\sin(\Delta\varphi)\cdot\left|\sin(\varphi_i)\right|}{4} \tag{15}$$

where $M_{k\text{-}1}$ and $\psi_{slab.k\text{-}1}$ is the unbalanced moment and the total rotation due to slab deformation at the load step k-1.The last fraction of Eq. (14) is inserted so that the sum of the width of all effective beams yields the width of one single effective beam that represents the slab action (Effective Beam Width Method).

The radial and torsional moments $M_{rad}(\varphi_i, r_s)$ and $M_{tor}(\varphi_i, r_s)$ at the perimeter of each sector element can be found by projecting the moment calculated using Eq. (14) to the radial and tangential direction, respectively:

$$M_{tor}(\varphi_i, r_s)=M_{y.\,EBW}(\varphi_i)\cdot\cos(\varphi_i) \tag{16}$$

$$M_{rad}(\varphi_i, r_s)=M_{y.\,EBW}(\varphi_i)\cdot\sin(\varphi_i) \tag{17}$$

Figure 6 shows the distribution of radial and torsional moments at the slab perimeter for a case study for ψ_{slab} = 1%.

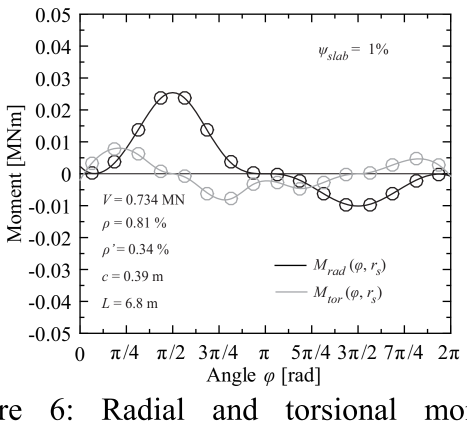

Figure 6: Radial and torsional moment distribution at the slab perimeter.

3.4 Failure criterion

In the following, two failure criteria for drift-induced punching are proposed, which are both based on the failure criterion of the CSCT [5]. One failure criterion is applied to slabs subjected to monotonic loading and the other to slabs subjected to cyclic loading. The criteria differ with regard to the assumed shear force redistribution. Shear redistribution from sector elements with higher rotations to sector elements with smaller rotations has been previously found to influence significantly the punching strength [8] and corresponding rotation of slabs loaded and/or reinforced in a non-axisymmetric manner.

For slabs subjected to monotonic loading, it is assumed that failure occurs when the shear force reaches the shear resistance for the hogging slab half. This criterion is denoted by CSCT(mono). For slabs subjected to cyclic loading, shear redistribution is neglected and failure assumed to occur when the sector subjected to the largest slab rotation reaches the CSCT-failure criterion. This is denoted by CSCT(cyc). In the following, the two failure criteria are described.

The failure criterion CSCT(cyc) applied to cyclically loaded slabs predicts smaller rotation capacities than the failure criterion CSCT(mono) applied to monotonically loaded slabs. Cyclic loading leads to an accumulation of plastic strains and therefore to an increase in crack opening with each cycle. If symmetric cycles are applied, ψ_{min} increases with increasing number of cycles. For the same slab rotation ψ_{scc}, ψ_{max} is therefore larger and so are the crack widths of the hogging slab half, which in turn lead to a reduced shear force redistribution between adjacent sector elements. To account for this phenomenon implicitly, different failure criteria are applied to monotonically and cyclically loaded slabs. This implicit approach is chosen since the analytical model does not account for the effect of the loading history on the moment-rotation relationship.

- *Approach accounting for shear stress redistribution (CSCT(mono))*

Based on the work of Sagaseta et al. [8] on non-axisymmetric punching it is assumed that failure of monotonically loaded slabs occurs when the sum of the shear forces acting on the sector elements of the hogging slab half ($0 \leq \varphi \leq \pi$) is equal to the sum of the shear resistance of these sector elements:

$$V_{R.hog} = \int_0^{\pi} v_R(\varphi) \cdot (r_c + d(\varphi))\, d\varphi \tag{18}$$

where the shear resistance per unit length in MN/m is

$$v_R(\varphi) = \frac{0.75 \cdot d(\varphi) \cdot \sqrt{f_c'}}{1 + 15 \cdot \dfrac{\psi(\varphi) \cdot d(\varphi)}{d_g + d_{g.0}}} \quad \text{(SI Units; N, mm)} \tag{19}$$

where f_c is the concrete compressive strength, d_g is the maximum aggregate size and $d_{g.0}$ is the reference aggregate size, which is assumed to be equal to 16mm. Note that the effective depth d changes with φ to account for the different effective depths for bending around the x- and y-axis. One can either apply a cosinusoidal interpolation for intermediate angles or use an average value for all angles. The former is applied for the calculations presented in this report.

- *Approach based on the maximum rotation (CSCT(cyc))*

In this report, the CSCT(cyc) approach is used for slabs subjected to cyclically increasing moment. This approach neglects a possible redistribution of the shear force to adjacent sector elements, which are subjected to smaller rotations than the maximum rotation ψ_{max}. It is assumed that punching failure occurs when the shear force that is carried by the compression strut (that is developed along the shear crack) of the sector element with the maximum rotation ψ_{max} is equal to the shear resistance of this sector element. According to the CSCT [5] the shear resistance of the sector element subjected to the maximum rotation ψ_{max} can be computed as:

$$V_{R.\pi/2}=\frac{0.75 \cdot b_0(\Delta\varphi) \cdot d(\pi/2) \cdot \sqrt{f_c{}'}}{1+15 \cdot \dfrac{\psi_{max} \cdot d(\pi/2)}{d_g+d_{g.0}}} \quad \text{(SI Units; N, mm)} \tag{20}$$

where $b_0(\Delta\varphi)$ is the part of the critical section that belongs to the sector element with the maximum rotation. The critical section is assumed to be at a distance of $d/2$ from the column face.

3.5 Experimental validation

The developed model was compared to punching shear tests on slabs that are reported in the literature. In Appendix I the adopted setup configurations are briefly presented and the definition of the connection rotation ψ_{scc} with respect to the proposed model is discussed for each case. More information on the selected tests is provided in Appendix II (Tables 1 and 2). In Appendix III, the proposed model for the moment-rotation relationship is compared to experimental moment-rotation curves found in literature conducted both under monotonic and cyclic loading conditions. For most tests, the proposed model for the moment-rotation relationship was found to be in good agreement with the experimental moment-rotation curves. In Appendix IV, the full model (moment-rotation relationship and failure criterion) is compared to tests found in the literature in terms of moment and deformation capacity. In the present section, the overall performance of the full model in terms of moment and deformation capacity is presented and discussed. For all isolated specimens, the moment-rotation relationship was calculated using $r_s = 0.22L$. For tests where the vertical load was applied on the slab surface, the radius of the specimen is equal to $0.50L$. For these cases (represented by square markers), the radial and tangential moments acting on the perimeter of the sector elements were not set to zero to account for the influence of the outer region of the slab on the moment-rotation response. For all other cases (represented by round markers), $0.22L$ corresponds to the specimen radius and, therefore, the radial and tangential moments acting on the slab perimeter were set to zero.

Figure 7 shows that the model predicts the moment capacity of the slab-column connection rather well for both monotonic and cyclic tests. The ratio of predicted to observed values was 1.018±0.107 for monotonic tests conducted under constant vertical load (Figure 7a), 0.964±0.067 for cyclic tests conducted under constant vertical load (Figure 7b), and 1.012±0.103 for monotonic tests conducted under constant eccentricity (Figure 7c).

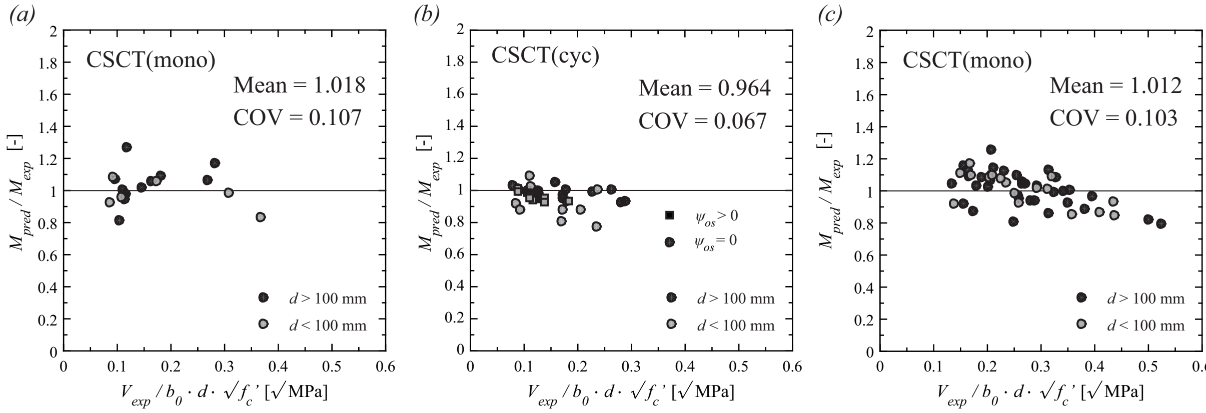

Figure 7: Moment resistance predictions according to the proposed model for specimens subjected to: (a) constant shear force and monotonically increasing moment (CSCT(mono)), (b) constant shear force and cyclically increasing moment (CSCT(cyc)); and (c) constant eccentricity and monotonically increasing shear force (CSCT(mono)).

For seismic loading, the deformation capacity is as important as the moment capacity. Figure 8 shows the comparison of the peak rotations predicted by the proposed model to the peak rotations observed during tests. For slabs subjected to constant vertical load the comparison with the proposed model was performed in terms of slab-column connection rotation (ψ_{scc}) and rotation due to slab deformation (ψ_{slab}) for specimens with $r = 0.22L$ and $r = 0.50L$, respectively. The ratio of predicted to observed values was 0.899±0.205 and 0.963±0.132 for monotonic loading conditions (Figure 8a) and cyclic loading conditions (Figure 8b), respectively. For monotonic tests carried out under constant eccentricity, only maximum slab rotations ψ_{max} were reported for the tests documented in the literature. The comparison with the proposed model was therefore performed at a local level. The ratio of predicted to observed values was 0.985±0.131 (Figure 8c).

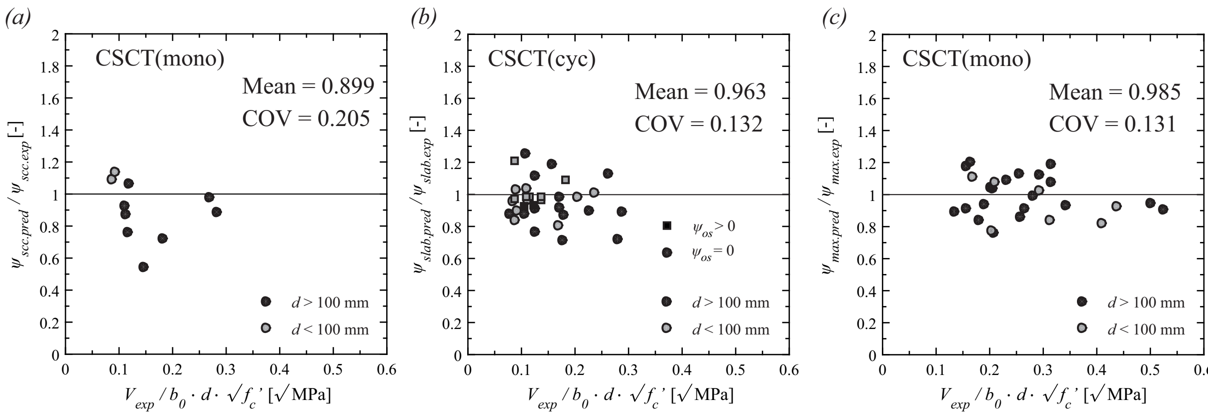

Figure 8: Deformation predictions according to the proposed model for (a) monotonic tests under constant shear force (ψ_{scc}); (b) cyclic tests under constant shear force (ψ_{slab}); and (c) monotonic tests under constant eccentricity (ψ_{max}).

A more extensive comparison of predicted and experimentally determined rotation and moment capacities can be found elsewhere [2;3]. In these studies, the influence of gravity loads, reinforcement ratios and load eccentricity on the goodness of fit of the prediction/rotation and moment capacity of the slab are discussed.

4. Seismic actions on slab-column connections

For adequate earthquake-resistant design and seismic assessment of a structure, its dynamic properties (stiffness, mass, and damping) should be known in order to accurately estimate the lateral loads that are introduced to each member of the structure. For reinforced concrete structures, stiffness and damping depend on the applied loads as well as the history of the earthquake event. The design process requires iterations on the used members (columns, beams, shear walls, etc.) and their dimensions to ensure safety and cost. In Switzerland, this process often involves the use of beamless floor systems, commonly referred to as flat slabs. To define the seismic moment introduced on a slab-column connection and the corresponding interstory drift, the stiffness of both the slab and the column should be known beforehand, taking into consideration the nonlinear behaviour of both members. For the column, the effective stiffness as defined by Priestley et al. [7] has shown good performance in comparison to test results and is usually used for seismic analysis. The physical model presented in the previous section can be used to estimate the stiffness of the slab in the proximity of the slab-column connection as well as the connection rotation for a given inserted moment.

A simplified analysis method for buildings with slab-column connections was developed based on the proposed analytical model. The method is suitable only if the slab-column connections are not part of the lateral force-resisting system (LFRS) of the building and requires iterations for calculating the contributions of column and slab deformation on the interstory drift from analysis, as described in the following:

1. Numerical analysis of the members that are part of the LFRS and calculation of the story drift demand at the slab-column connection of interest (Figure 9b).
2. Choice of the percentage of the column deformation contributing to the interstory drift as calculated at Step 1.
3. Calculation of the moment *M* at the column ends due to column deformation. This is the moment that is introduced to the slab-column connection.
4. Calculation of the rotation due to slab deformation ψ_{slab} that is corresponding to the inserted moment *M* from the proposed model.
5. Revision of the drift due to column deformation using the following formula:

$$\psi_{col}=\psi_{st}-\psi_{slab} \tag{21}$$

6. Repetition of the calculation of Steps 2 through 5 until convergence between new ψ_{col} and old ψ_{col} is reached.

A limited number of iterations (less than 10) is required to reach convergence. This approach presents the advantage that only one numerical analysis is performed. However, it can be applied only to gravity columns, i.e. columns that are not part of the LFRS.

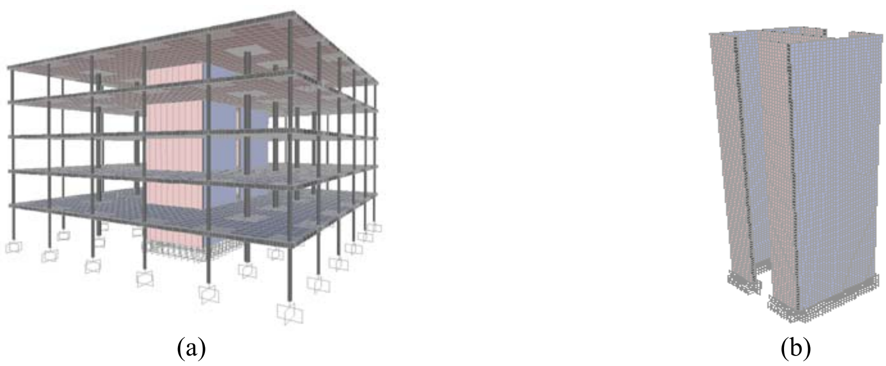

(a) (b)

Figure 9: Typical numerical models for seismic analysis of buildings with slab-column connections for (a) full structure, and (b) proposed method (lateral-force-resisting system).

5. Vulnerability classification of Swiss buildings with slab-column connections

Based on the tools presented above, the vulnerability classification of Swiss buildings with flat slabs was performed. Since flat slabs are mostly employed in administrative and industrial buildings in which lateral stability is conferred by a stiff vertical spine, the case of buildings with moment-resisting frames as stabilizing systems was not treated in the present report. In addition, preliminary analyses of cases with abrupt LFRS stiffness changes along height showed that the obtained results were significantly dependent on the stiffness change and therefore were not considered in the following. The vulnerability classification was thus performed for cases with or without eccentricity of the LFRS with regard to the center of mass of the building and for two seismic zones of Switzerland, Z1 (low seismicity) and Z3b (highest seismicity in Switzerland, medium seismicity compared to other regions in Europe and the World) [8].

The building that served as a basis for the analyses was constructed on the EPFL campus, Lausanne in 2010. For the project's purposes, the building was redesigned in order to not include transverse reinforcement in the proximity of the slab-column connections and to propose a LFRS as flexible as possible in order to resist the seismic forces according to SIA 262/2013 [10]. Using this procedure for the original building (Figure 10a) came out the case study buildings of Figure 10c.

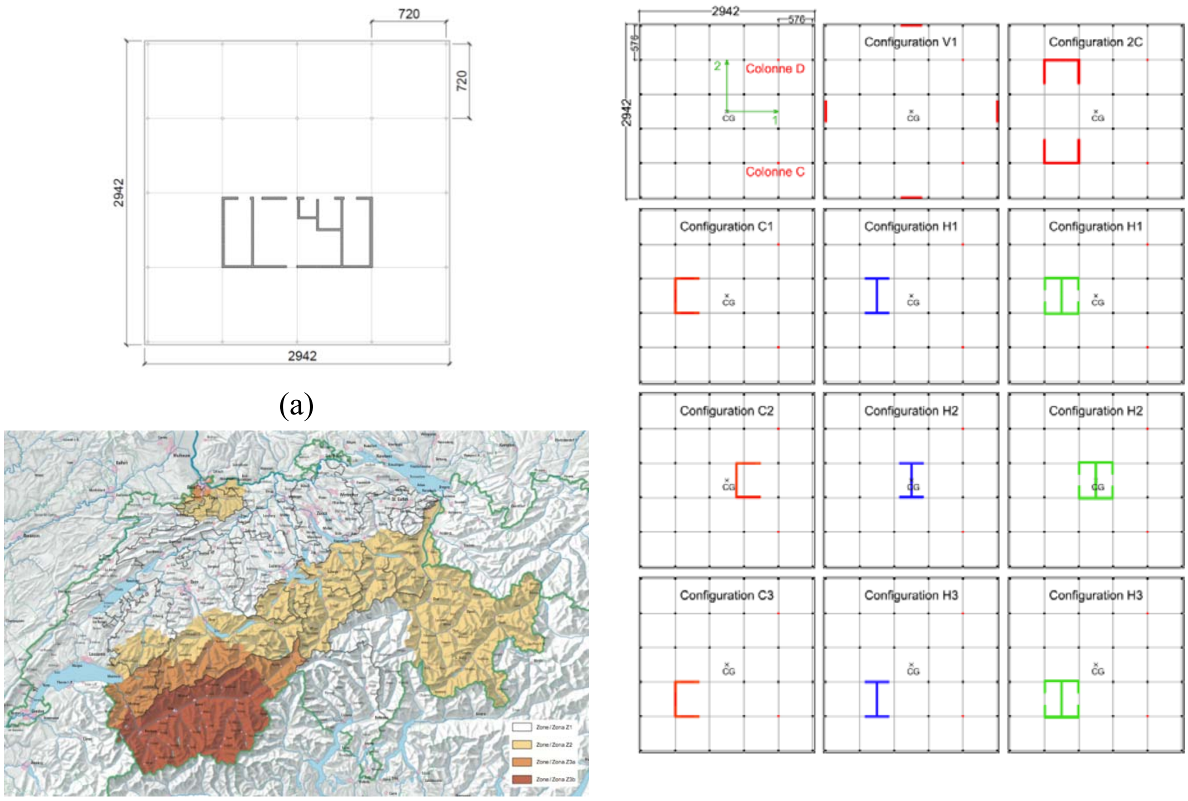

(a) (b) (c)

Figure 10: (a) Plan view of the reference building (dimensions in cm), (b) Seismic risk zones of Switzerland (SIA 261–Annexe F), and (c) examined configurations (in terms of form and eccentricity of the LFRS) for seismic zones Z1 (left and central column), and Z3b (right column).

5.1 Interstory drift demand

To assess the seismic vulnerability, firstly the relative displacement between adjacent floors (termed as interstory drift) was calculated at the position of the slab-column connections of interest (corresponding to interior columns C and D in Figure 10c). For the sake of simplicity and since the slab-column connections do not belong to the LFRS, the method proposed in Section 4 was used.

The influence of the form and position of vertical spines on the interstory drift profile along the height is examined in this subsection. The results for Direction 2 of the building (see Figure 10c) for which the higher interstory drifts were calculated are presented in Figure 11a and Figure 11b for ductile (q =4) and conventional design (q =2), respectively (Z3b is on the left and Z1 is on the right) using the response spectrum method. The maximum interstory drift can be rapidly estimated by considering the spectral displacement that corresponds to the first mode per direction and assuming for the sake of simplicity that is concentrated in one single story. If the LFRS does not coincide with the centre of mass of the building, the displacement due to in-plane rotation $\theta_z \cdot (x_{col} - x_s)$ should be added to the displacement calculated using this simplified method to account for the eccentricity between the centre of stiffness and the centre of mass, where x_s and x_{col} are the coordinates of the centre of stiffness and the column of interest.

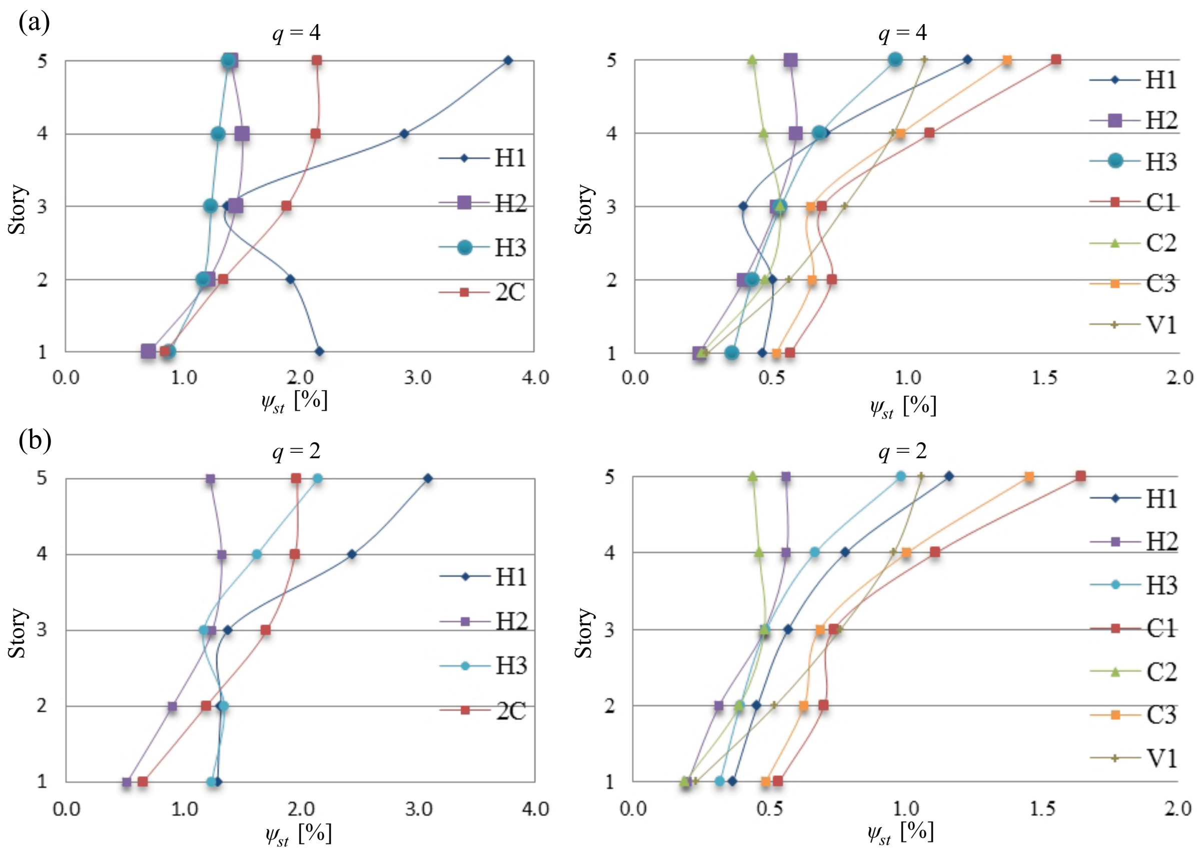

Figure 11: Results for the influence of regularity in plan on interstory drift maximum value and profile in height for seismic zones Z3b (left) and Z1 (right) according to (a) ductile design (q =4), and (b) conventional design (q =2).

5.2 Seismic assessment of slab-column connections

On the basis of the previous results, the assessment of the slab-column connections was performed. The iterative procedure presented in Section 4 was used to calculate the connection rotation from the interstory drift values shown in Figure 11. The column stiffness was assumed to be equal to 50% of the gross section stiffness to take into account cracking.

The CSCT(cyc) was applied, since it gives more conservative results than the CSCT(mono) approach for monotonic loading and rather accurate results for cyclic loading. The cases that yielded the larger inserted moment in the slab-column connections of interest were:

- Story level 4 of configuration H1 (q =4) for Z3b. The interstory drift of the floor above is 3.65% and the interstory drift of the floor below is 2.89%.
- Story level 4 of configuration C1 (q =2) for Z1. The interstory drift of the floor above is 1.65% and the interstory drift of the floor below is 1.11%.

The results show that even with maximum drift, structural safety is guaranteed. The safety margin is relatively large for seismic zone Z1 both for moment resistance and deformation capacity (63% and 83%, respectively). For zone Z3b, as expected, the safety margin is smaller (18% for moment resistance and 25% deformation capacity).

The results of the seismic evaluation are summarized in Tables 1 and 2 for H-shaped and C-shaped core walls, respectively (L_b is the building dimension in plan—see Figure 10a). Arranging the stabilizing system with zero eccentricity with respect to the center of mass of the building increased the safety margin compared to the case with $e = L_b/4$ in one of the two principal building directions, particularly for Z3b (approximately 3.5 times for both moment resistance and deformation capacity). Moreover, eccentricity of the LFRS in both directions did not lead to higher seismic vulnerability of the slab-column connections. Adoption of a C-shaped instead of a H-shaped core wall for the low seismicity zone Z1 decreased the safety margin by only 11% for resistance and 7% for deformation capacity.

> 60 %	60 % - 20 %	20 % - 0 %	No safety

Table 1–Safety margins of interior slab-column connections for the design level earthquake (H-shaped core wall)

Moment resistance						Deformation capacity					
Ductile design			Conventional design			Ductile design			Conventional design		
Z1											
e_y \ e_x	0	$L_b/4$	e_y \ e_x	0	$L_b/4$	e_y \ e_x	0	$L_b/4$	e_y \ e_x	0	$L_b/4$
0	74%	74%	0	73%	74%	0	91%	91%	0	89%	90%
$L_b/4$	74%	78%	$L_b/4$	74%	77%	$L_b/4$	91%	92%	$L_b/4$	90%	92%
Z3b											
e_y \ e_x	0	$L_b/4$	e_y \ e_x	0	$L_b/4$	e_y \ e_x	0	$L_b/4$	e_y \ e_x	0	L_b /4
0	61%	18%	0	66%	31%	0	82%	25%	0	86%	44%
$L_b/4$	18%	49%	$L_b/4$	31%	47%	$L_b/4$	25%	72%	$L_b/4$	44%	70%

Table 2–Safety margins of interior slab-column connections for the design level earthquake (C-shaped core wall) for seismic zone Z1

Moment resistance						Deformation capacity					
Ductile design			Conventional design			Ductile design			Conventional design		
Z1											
e_y / e_x	0	$L_b/4$	e_y / e_x	0	$L_b/4$	e_y / e_x	0	$L_b/4$	e_y / e_x	0	$L_b/4$
0	65%	65%	0	63%	63%	0	85%	85%	0	84%	83%
$L_b/4$	65%	68%	$L_b/4$	63%	67%	$L_b/4$	85%	87%	$L_b/4$	83%	86%

It should be noted that the aforementioned results are applicable to the specific geometry and height of the building and should therefore not be extrapolated to different heights or different building and member geometries. In that case, the approach presented in Section 4 should be used by the structural engineer.

6. Conclusions

A physical model for the moment-rotation relationship of slab-column connections under seismically induced deformations is proposed based on the axisymmetric model developed by Kinnunen & Nylander [5] and Muttoni [6]. The presented approach considers both the load and deformation of the slab respecting equilibrium both on a local level (sector elements) and a global level (specimen). The model combined with the failure criterion that accounts for shear redistribution (CSCT(mono)) has shown good performance when compared to monotonic tests found in the literature and performed by the research group for both the moment resistance and the deformation capacity. On the other hand, when the model was combined with the CSCT(cyc), both the moment resistance and the deformation capacity of cyclic tests were predicted accurately enough.

A rapidly converging iterative procedure based on the proposed model is proposed to estimate the contribution of the slab deformation to the interstory drift during an earthquake. This tool combined with the CSCT(cyc) (to take into account the cyclic effect) can be used by engineers to design buildings with slab-column connections as well as to assess existing buildings, taking into account seismically-induced deformations.

The seismic vulnerability of a typical administrative Swiss building with slab-column connections was assessed and various case studies were examined to investigate the effect of eccentricity of the LFRS and the seismic zone on the assessment result. All analysed buildings were braced by walls that are continuous from the foundation to the top storey. For these cases, the structural safety of the slab-column connections is guaranteed. The safety margins for both moment resistance and deformation capacity are relatively large for zone Z1 (63% and 83%, respectively), but significantly smaller for zone Z3b (18% for moment resistance and 25% for deformation capacity). Arrangement of the LFRS with no eccentricity with respect to the center of mass has shown to be beneficial for the safety margins by approximately 3.5 times, compared to cases with moderate eccentricity of the LFRS ($e = L_b/4$).

The present report shows that for typical Swiss buildings up to 3-4 stories stabilized by properly designed shear walls, the structural safety of the slab-column connections is guaranteed with relatively large safety margins. However, for cases of increased building height, abrupt LFRS stiffness changes along height and larger eccentricities of the LFRS with respect to the centre of mass of the building, the seismic drift demand on the slab-column connections might lead to premature punching failure. In these cases, the proposed method can be used by the structural engineer for the design or the assessment of the building.

7. Recommendations for further research

The use of shear reinforcement has shown to improve the seismic behaviour of slab-column connections with respect to both moment resistance and deformation capacity. Therefore, it should be further investigated to which extent shear reinforcement in the proximity of the slab-column connection can enhance its seismic behaviour and whether such a choice could guarantee the structural safety of Swiss buildings with flat slabs including those with stiffness irregularities in plan and/or in elevation, increased height. This would have the advantage that engineers would no longer need to check the seismic capacity of slab-column connections with shear reinforcement for any building in Switzerland. To this end, the model proposed in this present report should be extended for slabs with shear reinforcement.

8. Funding

For the performed project the following financing is desired, which was calculated on the basis of common CTI approaches:

Project Management	80 h	105.- CHF /h	8'400.-
(Prof. A. Muttoni, Prof. K. Beyer)			
Scientific Assistance	1'120 h	60.- CHF/h	67'200.-
(Ioannis-Sokratis Drakatos)			
TVA			0.-
Total amount requested			CHF 75'600

Bibliography

[1] **ACI**, *ACI 318-2014, ACI Building Code Requirements for Structural Concrete and Commentary*, American Concrete Institute, Farmington Hills, Michigan, U.S.A., **2014**.

[2] **DRAKATOS I.-S., MUTTONI A. and BEYER K.**, *Mechanical model for flexural behaviour of slab-column connections under seismically-induced deformations*, 4th FIB Congress, Mumbai, India, **2014**.

[3] **DRAKATOS I.-S., BEYER K. and MUTTONI A.**, *Lateral force resisting mechanisms in slab-column connections: An analytical approach*, 2nd European Conference of Earthquake Engineering and Seismology, Istanbul, Turkey, **2014**.

[4] **DRAKATOS I.-S., MUTTONI A. and BEYER K.**, *Mechanical model for drift-induced punching of slab-column connections without transverse reinforcement*, ACI Structural Journal, U.S.A, **2015** (Under preparation)

[5] **KINNUNEN S., NYLANDER H.**, *Punching of concrete slabs without shear reinforcement*, Transactions of the Royal Institute of Technology, N° 158, 112 p., Sweden, **1960**.

[6] **MUTTONI A.**, *Punching shear strength of reinforced concrete slabs without transverse reinforcement*, ACI Structural Journal, V. 105, N° 4, pp. 440-450, U.S.A, **2008**.

[7] **PRIESTLEY M.J.N., CALVI G.M. and KOWALKSY M.J.**, *Displacement-Based Seismic Design of Structures*, IUSS Press, Pavia, Italy, 670 p., **2007**.

[8] **SAGASETA J., FERNÁNDEZ RUIZ M., MUTTONI A. and TASSINARI L.**, *Non-axis-symmetric punching shear around internal columns of RC slabs without transverse reinforcement*, Magazine of Concrete Research, Vol. 63, pp. 441-457, United Kingdom, **2011**.

[9] **SEDILI I.**, *Evaluation sismique de bâtiments en béton armé comportant des connexions dalle-colonne*, M.Sc. Thesis, EPFL, Lausanne, Switzerland, French, **2014**.

[10] **SIA**, *SIA 262:2013, Construction en béton*, Société Suisse des Ingénieurs et des Architectes, Norme suisse SN 505 262, **2013**.

APPENDIX I: Test setups for experimental investigation of flat slabs under seismically-induced deformations

For tests on a single interior slab-column connection different test setups were developed concerning the slab and column boundary conditions as well as the way lateral loads were simulated. However, all test setups can be assigned to one of the following three schemes (Figure 12 and Figure 13):

- Test setup (a): the unbalanced moment is introduced by an eccentric vertical load and by restraining the vertical displacement of the slab ends (Figure 12a).
- Test setup (b): the unbalanced moment is introduced by applying unequal vertical loads to the ends of the slab and by restraining the horizontal displacement of the column stub ends (Figure 12 and Figure 13).
- Test setup (c): the unbalanced moment is introduced by applying a horizontal force to the top column stub and by restraining the vertical displacement of the slab edges (Figure 12 and Figure 13). The vertical load is applied either by jacks underneath the column stub (monotonic tests - Figure 12) or by weights on the slab surface (cyclic tests – Figure 13).

The setup configuration adopted in each test campaign is indicated in brackets after the researcher's name is Tables 1, 2 and 3 (Appendix II).

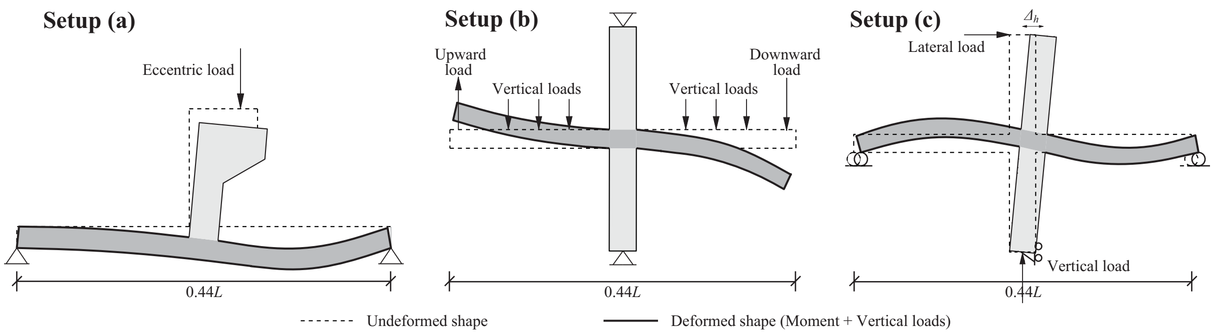

Figure 12: Test setup configurations used in previous experimental campaigns for slab-column connections with monotonic moment transfer

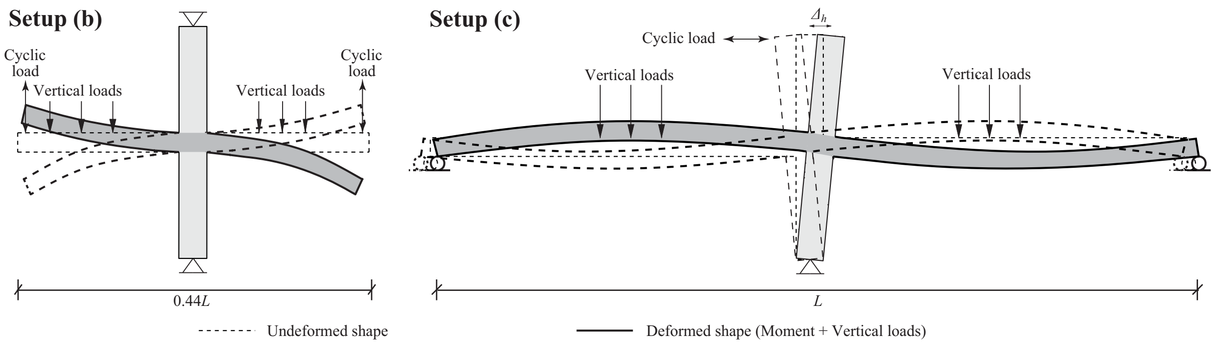

Figure 13: Test setup configurations used in previous experimental campaigns for slab-column connections with cyclic moment transfer

In the following the definition of the slab-column connection rotation for the setups that are most suitable for simulating seismically-induced deformations (setups (b) and (c)) is briefly discussed. The deformed shape of the slab for each setup is also shown in the following sections.

Setup (b)

For setup (b) the deformed shape of the slab under vertical loads, lateral loads and combined vertical and lateral loads is shown in Figure 14. The deformed shape assumed by the proposed model is also shown in the same figure.

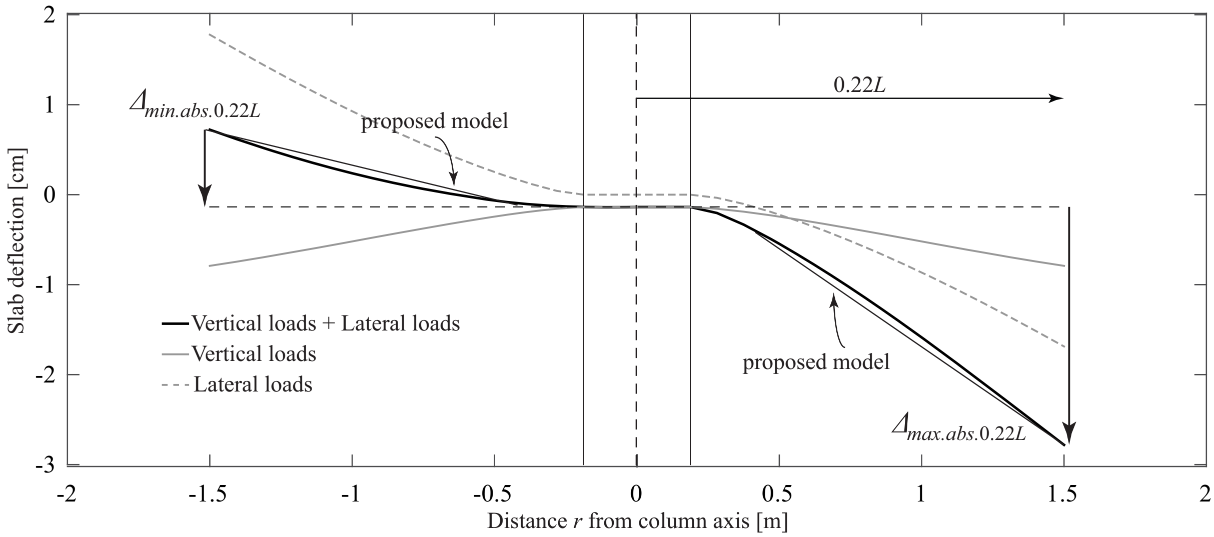

Figure 14: Setup (b)—Deformed shape of slab according to finite element analysis and the proposed model.

Therefore, for this setup configuration the connection rotation can be calculated either based on rotations:

$$\psi_{scc.rot}=\frac{\psi_{max}-\psi_{min}}{2}=\frac{\Delta_{max}-\Delta_{min}}{2\cdot\Delta r} \tag{22}$$

or on deflections:

$$\psi_{scc.defl}=\frac{\Delta_{max}-\Delta_{min}}{2\cdot\Delta r+c} \tag{23}$$

Finite element analyses have shown that, for this setup configuration, calculation of the connection rotation on the basis of deflections provides more realistic estimation of the interstory drift of an internal connection of the reference slab-column frame [4]. This definition was therefore used both for the experimental peak connection rotations (Appendix II) and the predicted peak connection rotations (Appendix IV) for the slabs tested using this setup.

Setup (c)

For setup (c) the deformed shape of the slab depends on the way the vertical loads are applied. For vertical loads applied by jacks underneath the column stub (Figure 15) the deformed shape resembles the deformed shape for setup (b) (Figure 14); for vertical loads applied on the slab surface (Figure 16) the deformed shape is significantly different since the slab region between r =0.22L and 0.50L contributes to the slab deformation under vertical loads, lateral loads and combined vertical and lateral loads is shown in Figure 15 until midspan (0.50L).

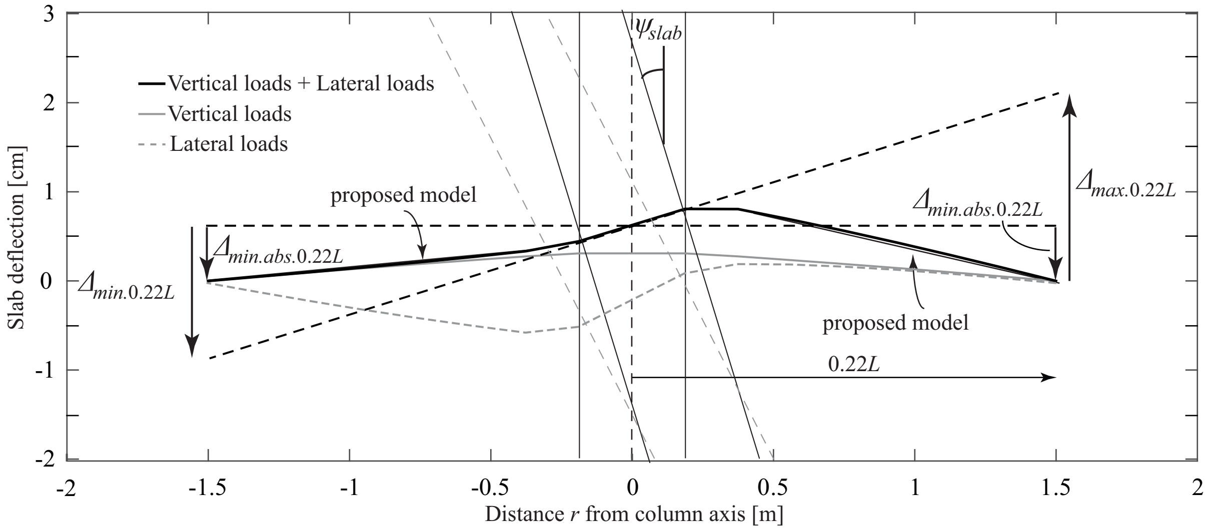

Figure 15: Setup (c) with vertical load applied on the column: Deformed shape of slab according to finite element analysis and the proposed model.

According to the proposed model the slab-column connection rotation based on rotations is:

$$\psi_{scc.rot} = \frac{\psi_{max}-\psi_{min}}{2} = \frac{(\Delta_{max.abs}+\psi_{st}\cdot\Delta r)}{2\cdot\Delta r} - \frac{(\Delta_{min.abs}-\psi_{st}\cdot\Delta r)}{2\cdot\Delta r} = \frac{(\Delta_{max.abs}-\Delta_{min.abs})}{2\cdot\Delta r} + \psi_{st} \tag{24}$$

The connection rotation based on deflections is:

$$\psi_{scc.defl} = \frac{\Delta_{max}-\Delta_{min}}{2\cdot\Delta r+c} = \frac{(\Delta_{max.abs}+\psi_{st}\cdot\Delta r)}{2\cdot\Delta r+c} - \frac{(\Delta_{min.abs}-\psi_{st}\cdot\Delta r)}{2\cdot\Delta r+c} = \frac{\Delta r}{2\cdot\Delta r+c}\cdot\psi_{st} \tag{25}$$

For setup (c) with the vertical load applied on the column, since the deflections of the tip of the hogging and sagging slab half relative to the column center ($\Delta_{max.abs}$ and $\Delta_{min.abs}$ respectively) are equal (Figure 15), the connection rotation that is calculated according to the proposed model based on rotations is equal to the interstory drift (with zero rotation due to column deformation). Therefore, this last definition of connection rotation – ($\psi_{scc.rot}$ - Eq. (12)) will be used for the comparison of the proposed model with experimentally measured interstory drift for tests using setup (c) (Appendix IV).

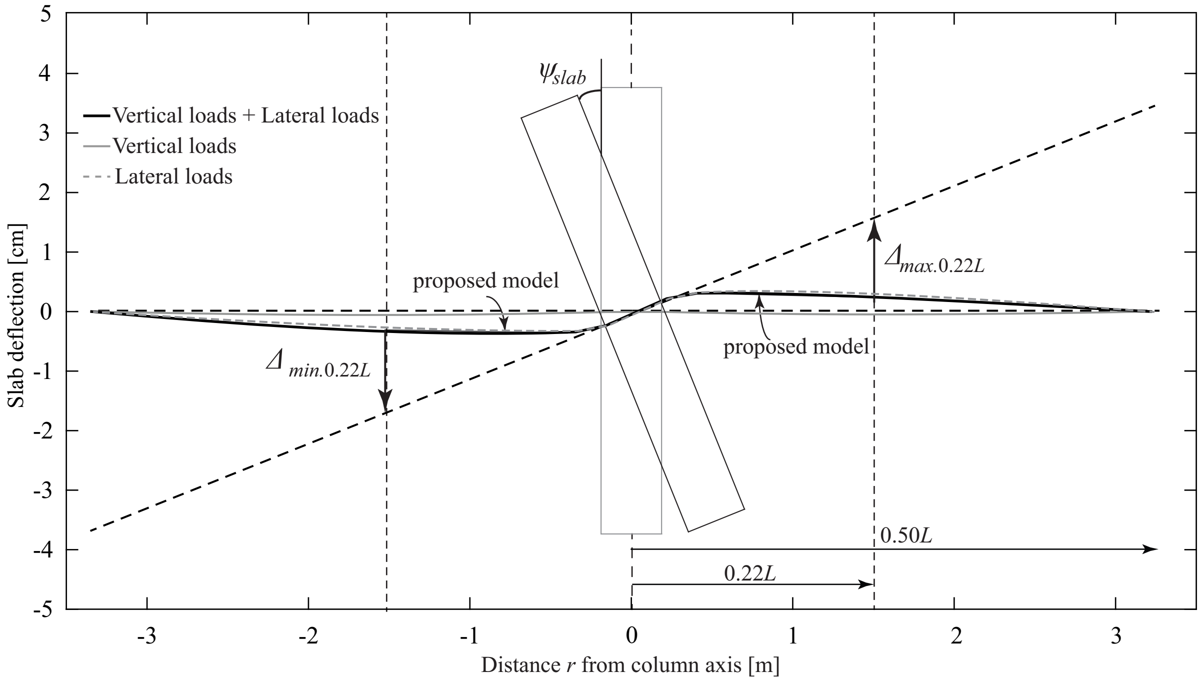

Figure 16: Setup (c) with vertical load applied of the slab surface: Deformed shape of slab according to finite element analysis and the proposed model.

For setup (c) with the vertical load applied on the slab surface, since the slab part between 0.22L and 0.50L contributes to the rotation due to slab deformation ψ_{slab}, the connection rotation that is calculated according to the proposed model is smaller than the interstory drift (with zero rotation due to column deformation). For this case, an effective beam model is established in order to calculate the contribution of the slab part outside 0.22L to the interstory drift.

It should be mentioned that for the experimental investigation using the setups that are the most suitable for simulating seismically-induced deformations ((b) and (c)) a contribution of column deformation to the interstory could occur. However, for setup (b) the column was most times post-tensioned to reduce column deformation (e.g. [4]) and for setup (c) the column was typically designed to remain elastic during the moment introduction. Nevertheless for both setups the contribution of column deformation was measured by most researchers and subtracted from the measured global slab rotation.

APPENDIX II: Test database

Table APP-II- 1: Summary of properties, dimensions and results of interior isolated slab specimens tested under constant vertical load and monotonically increasing moment

Slab	Geometric properties				Material properties			Reinforcement content		Loading parameters	Results	
	c [mm]	h [mm]	d [mm]	B [m]	f_c [MPa]	d_g [mm]	f_y [MPa]	ρ [%]	ρ' [%]	$V_{test}/b_0 \cdot d \cdot \sqrt{f_c}$ $[\sqrt{MPa}]$	M_{peak} [kNm]	$\psi_{scc.peak}$ [%]
Ghali et al, 1974 (c)												
B3NP	305	152	114	1.81	23.7	16.0	345	1.39	1.39	0.114	162.0	-
B5NP	305	152	114	1.81	28.3	16.0	345	1.39	1.39	0.104	196.0	-
Stamenkovic and Chapman, 1974 (c)												
C/I/1	127	76	56	0.87	36.0	9.5	434	1.17	1.17	0.368	7.3	-
C/I/2	127	76	56	0.87	29.7	9.5	434	1.17	1.17	0.308	10.5	-
C/I/3	127	76	56	0.87	25.9	9.5	434	1.17	1.17	0.174	13.6	-
C/I/4	127	76	56	0.87	25.4	9.5	434	1.17	1.17	0.108	16.7	-
Ghali et al, 1976 (c)												
SM0.5	305	152	120	1.83	36.8	16.0	476	0.50	0.18	0.111	100.0	3.60
SM1.0	305	152	120	1.83	33.4	16.0	476	1.05	0.33	0.116	128.0	2.63
SM1.5	305	152	120	1.83	39.9	16.0	476	1.35	0.39	0.107	132.0	2.10
Islam and Park, 1976 (b)												
IP1	229	89	70	2.24	27.3	6.0	356	0.83	0.43	0.092	30.5	3.62
IP2	229	89	70	2.24	31.9	6.0	374	0.83	0.43	0.085	37.7	3.97
Elgabry and Ghali, 1987 (c)												
1	250	152	123	1.80	35.0	16.0	452	1.10	0.43	0.163	130.0	-
Drakatos et al., 2015 (b)												
PD1	390	250	204	3.00	37.9	16.0	559	0.79	0.35	0.096	526.0	-*
PD3	390	250	198	3.00	34.9	16.0	558	0.81	0.34	0.269	200.0	0.45
PD4	390	250	201	3.00	39.0	16.0	507	0.80	0.35	0.112	527.5	2.01
PD5	390	250	198	3.00	37.5	16.0	507	0.81	0.35	0.146	462.0	2.19
PD10	390	250	197	3.00	32.3	16.0	593	1.60	0.72	0.281	290.0	0.49
PD12	390	250	195	3.00	35.5	16.0	546	1.61	0.72	0.181	469.0	1.21

*Inconsistent rotation measurement

Table APP-II- 2: Summary of properties, dimensions and results of interior isolated slab specimens tested under constant eccentricity and monotonically increasing moment

Slab	Geometric properties				Material properties			Reinforcement content		Loading parameters	Results	
	c [mm]	h [mm]	d [mm]	B [m]	f_c [MPa]	d_g [mm]	f_y [MPa]	ρ [%]	ρ' [%]	Eccentricity [mm]	V_{peak} [kN]	$\psi_{max.p}$ [%]
Elstner and Hognestad, 1956 (a)												
A11	356	152	114	1.83	25.9	25.4	326	2.47	1.15	178	529.0	1.39
A12	356	152	114	1.83	28.4	25.4	326	2.47	2.47	178	529.0	1.39
Moe, 1961 (a)												
M2	305	152	114	1.83	25.7	9.5	481	1.50	-	196	292.2	-
M2A	305	152	114	1.83	15.5	9.5	481	1.50	-	185	212.6	-
M3	305	152	114	1.83	22.8	9.5	481	1.50	-	338	207.3	-
M4A	305	152	114	1.83	17.7	9.5	481	1.50	-	434	143.7	-
M6	254	152	122	1.83	26.5	9.5	327	1.34	-	168	239.3	-
M7	254	152	122	1.83	25.0	9.5	327	1.34	-	61	311.0	-
M8	254	152	122	1.83	24.6	9.5	327	1.34	0.57	437	149.5	-
M9	254	152	122	1.83	23.2	9.5	327	1.34	-	127	266.9	-
M10	254	152	122	1.83	21.1	9.5	327	1.34	0.57	308	177.9	-
Anis, 1970 (a)												
B3	203	102	76	1.47	30.4	9.5	331	2.19	-	94	191.3	-
B4	203	102	76	1.47	29.8	9.5	331	2.19	-	188	139.7	-
B5	203	102	76	1.47	29.0	9.5	331	2.19	-	313	125.4	-
B6	203	102	76	1.47	31.3	9.5	331	2.19	-	464	115.7	-
B7	203	102	76	1.47	33.8	9.5	331	2.19	-	737	69.8	-
Narasimhan, 1971 (a)												
L1	305	178	143	2.28	33.8	9.5	398	1.11	-	305	399.0	-
Hawkins et al., 1989 (b)†												
6AH	305	152	121	1.83	31.3	19.0	472	0.60	0.28	535	169.0	5.55
9.6AH	305	152	118	1.83	30.7	19.0	415	0.79	0.50	522	187.0	4.02
14AH	305	152	114	1.83	30.3	19.0	420	1.26	0.63	489	205.0	3.19
6AL	305	152	121	1.83	22.7	19.0	472	0.60	0.28	135	244.0	3.19
9.6AL	305	152	118	1.83	28.9	19.0	415	0.79	0.50	135	257.0	2.64
14AL	305	152	114	1.83	27.0	19.0	420	1.26	0.63	136	319.0	2.22
7.3BH	305	114	82	1.83	22.2	19.0	472	0.64	0.40	488	80.0	4.16
9.5BH	305	114	83	1.83	19.8	19.0	472	0.79	0.51	483	94.0	4.72
14.2BH	305	114	79	1.83	29.5	19.0	415	1.22	0.76	500	102.0	3.19
7.3BL	305	114	83	1.83	18.1	19.0	472	0.64	0.40	98	130.0	3.89
9.5BL	305	114	83	1.83	20.0	19.0	472	0.79	0.48	117	142.0	4.16
14.2BL	305	114	76	1.83	20.5	19.0	415	1.22	0.75	129	162.0	3.47
6CH	305	152	121	1.83	52.4	19.0	472	0.60	0.28	511	186.0	6.24
9.6CH	305	152	117	1.83	57.2	19.0	415	0.87	0.50	519	218.0	3.14
14CH	305	152	114	1.83	54.7	19.0	420	1.16	0.63	529	252.0	3.05
6CL	305	152	121	1.83	49.5	19.0	472	0.60	0.28	135	273.0	4.72
14CL	305	152	114	1.83	47.7	19.0	420	1.16	0.63	136	362.0	2.36
14FH	305	152	114	1.83	31.2	19.0	446	0.90	0.22	498	206.0	2.58
6FLI	305	152	120	1.83	25.9	19.0	472	0.59	0.27	119	227.0	3.15
10.2FLI	305	152	114	1.83	18.1	19.0	446	1.13	0.49	112	240.0	1.94
10.2FLO	305	152	114	1.83	26.5	19.0	446	0.77	0.49	121	290.0	2.78
10.2FHO	305	152	121	1.83	33.8	19.0	446	0.77	0.49	491	183.0	3.05
Kamaraldin, 1990 (a)												
SA1	150	80	64	2.00	33.0	10.0	640	0.55	0.55	52	105.0	-
SA3	150	80	64	2.00	36.0	10.0	640	0.55	0.55	100	85.0	-
SA4	150	80	64	2.00	32.0	10.0	640	0.55	0.55	336	49.0	-
SB2	150	80	62	2.00	28.0	10.0	640	1.00	1.00	360	61.0	-
Marzouk et al., 1996 (b)												
NHLS0.5	250	150	119	1.87	43.2	19.0	450	0.50	0.28	150	164.3	-

Slab	Geometric properties				Material properties			Reinforcement content		Loading parameters	Results	
	c [mm]	h [mm]	d [mm]	B [m]	f_c [MPa]	d_g [mm]	f_y [MPa]	ρ [%]	ρ' [%]	Eccentricity [mm]	V_{peak} [kN]	$\psi_{max.p}$ [%]
NHLS1.0	250	150	119	1.87	42.7	19.0	450	1.00	0.38	150	250.3	-
NNHS0.5	250	150	119	1.87	36.2	19.0	450	1.00	0.38	550	266.2	-
NHHS0.5	250	150	119	1.87	34.0	19.0	450	0.50	0.28	550	408.2	-
NHHS1.0	250	150	119	1.87	35.3	19.0	450	1.00	0.38	550	163.6	-
Krüger et al., 2000 (a)												
P16A	300	150	121	3.00	38.6	16.0	460	1.00	-	160	332.0	1.26
P32	300	150	121	3.00	30.4	16.0	460	1.00	-	320	270.0	0.76
Binici and Bayrak, 2005 (a)												
CE	150	75	57	1.02	24.1	9.5	455	1.38	0.70	150	95.6	2.25
Ben Sasi, 2012 (a)												
SI-1	180	80	60	1.00	28.1	12.0	335	1.40	1.40	280	65.0	-
SI-2	180	80	60	1.00	25.0	12.0	335	1.40	1.40	580	37.5	-

† Maximum slab rotations, calculated from edge deflections, are reported

Table APP-II- 3: Summary of properties, dimensions and results of interior isolated slab specimens tested under constant vertical load and cyclically increasing moment

Slab	Geometric properties				Material properties			Reinforcement content		Loading parameters		Results	
	c [mm]	h [mm]	d [mm]	B [m]	f_c [MPa]	d_g [mm]	f_y [MPa]	ρ [%]	ρ' [%]	$V_{test}/b_0 \cdot d \cdot \sqrt{f_c}$ [$\sqrt{\text{MPa}}$]	N [-]	M_{peak} [kNm]	$\psi_{scc.peak}$ [%]
Kanoh and Yoshizaki, 1975 (c)													
H9	200	100	80	1.80	22.4	9.5	361	0.70	0.70	0.111	5	33.0	2.00
H10	200	100	80	1.80	21.7	9.5	361	1.10	0.70	0.112	5	36.1	2.00
H11	200	100	80	1.80	19.6	9.5	361	1.10	0.70	0.236	5	25.2	1.00
Islam and Park, 1976 (b)													
IP3C	229	89	70	2.24	29.7	6.0	316	0.83	0.43	0.089		35.8	3.62
Morrison et al., 1983 (c)													
S5	305	76	61	1.83	34.9	9.5	340	1.03	1.03	0.085	5	36.0	4.70
Zee and Moehle, 1984 (c)													
INT	137	61	52	1.83	26.2	9.5	470	0.80	0.34	0.138	2	10.3	3.79†
Pan and Moehle, 1989 (c)													
AP1	274	122	101	3.66	33.3	10.0	472	0.76	0.26	0.125	2	61.8	1.60
AP3	274	122	101	3.66	31.7	10.0	472	0.76	0.26	0.078	2	95.0	3.14
Cao, 1993 (c)													
CD1	250	150	115	1.90	40.4	20.0	395	1.29	0.46	0.287	1	49.9	0.90
CD5	250	152	115	1.90	31.2	20.0	395	1.29	0.46	0.228	1	70.5	1.20
CD8	250	155	115	1.90	27.0	20.0	395	1.29	0.46	0.179	1	85.0	1.30
Robertson et al., 2002 (c)													
1C	254	115	95	3.00	35.4	9.5	420	0.75	0.36	0.088	2	58.5	3.52†
Stark et al., 2005 (c)													
C-02	305	115	82	2.44	30.9	19.0	454	1.42	0.51	0.205	3	43.1	2.30
Robertson and Johnson, 2006 (c)													
ND1C	254	114	89	3.00	29.6	9.5	525	0.52	0.36	0.088	3	42.3	4.99†
ND4LL	254	114	89	3.00	32.3	9.5	525	0.52	0.36	0.116	3	43.9	3.00†
ND5XL	254	114	89	3.00	24.1	9.5	525	0.52	0.36	0.184	3	31.1	1.99†
ND6HR	254	114	89	3.00	26.3	9.5	525	1.03	0.67	0.111	3	58.5	2.97†
ND7LR	254	114	89	3.00	18.8	9.5	525	0.45	0.36	0.137	3	30.0	2.99†
Choi et al., 2007 (c)													
S1	300	120	90	2.40	33.5	16.0	458	1.05	0.60	0.090	2	83.1	3.00
S2	300	120	90	2.40	41.3	16.0	458	1.05	0.60	0.169	2	67.7	2.91
S3	300	120	90	2.40	37.8	16.0	458	1.59	0.80	0.093	2	118.5	2.89
Park et al., 2007 (c)													
RI-50	300	132	116	3.40	32.3	16.0	392	0.72	0.27	0.123	3	83.6	3.47†
Kang and Wallace, 2008 (c)													
C0	254	152	130	2.90	38.6	9.5	452	0.49	0.11	0.109	1	84.1	1.85
Tian et al., 2008 (c)													
L0.5	406	152	127	3.66	25.6	9.5	469	0.61	0.25	0.126	3	121.0	1.52
Bu and Polak, 2009 (c)													
SW1	200	120	89	1.80	37.0	16.0	520	1.25	0.60	0.172	3	64.7	-*
SW5	200	120	89	1.80	45.0	16.0	520	1.25	0.60	0.234	3	65.1	-*
Cho, 2009 (c)													
Control	300	150	130	3.00	34.3	25.0	392	0.45	0.25	0.106	3	105.3	4.44
Choi et al., 2009 (c)													
SPB	355	152	106	4.20	34.1	16.0	440	1.24	0.35	0.106	5	137.4	3.68†
Park et al., 2012 (c)													
RCA	300	135	106	2.70	22.5	9.5	430	1.06	0.79	0.171	3	70.8	1.24
RCB	300	135	106	2.70	38.7	9.5	430	1.06	0.79	0.157	3	74.0	1.37
Drakatos et al., 2015 (b)													
PD2	390	250	198	3.00	36.9	16.0	558	0.81	0.34	0.262	2	196	0.36
PD6	390	250	199	3.00	38.3	16.0	507	0.81	0.30	0.170	2	372	0.86

Slab	Geometric properties				Material properties			Reinforcement content		Loading parameters		Results	
	c [mm]	h [mm]	d [mm]	B [m]	f_c [MPa]	d_g [mm]	f_y [MPa]	ρ [%]	ρ' [%]	$V_{test}/b_0 \cdot d \cdot \sqrt{f_c}$ $[\sqrt{\text{MPa}}]$	N [-]	M_{peak} [kNm]	$\psi_{scc.peak}$ [%]
PD8	390	250	198	3.00	32.7	16.0	575	0.81	0.29	0.126	2	384	1.30
PD11	390	250	196	3.00	33.1	16.0	593	1.60	0.71	0.280	2	286	0.43
PD13	390	250	196	3.00	36.5	16.0	546	1.60	0.72	0.178	2	410	0.86

†Rotation due to slab deformation ψ_{slab} for tests using setup (c) with the vertical load applied on the slab
*Inconsistent rotation measurement (communication with the authors)

APPENDIX III: Moment-rotation relationship evaluation

- **MONOTONIC TESTS**

➢ **Constant vertical load**

Ghali et al. (1976)

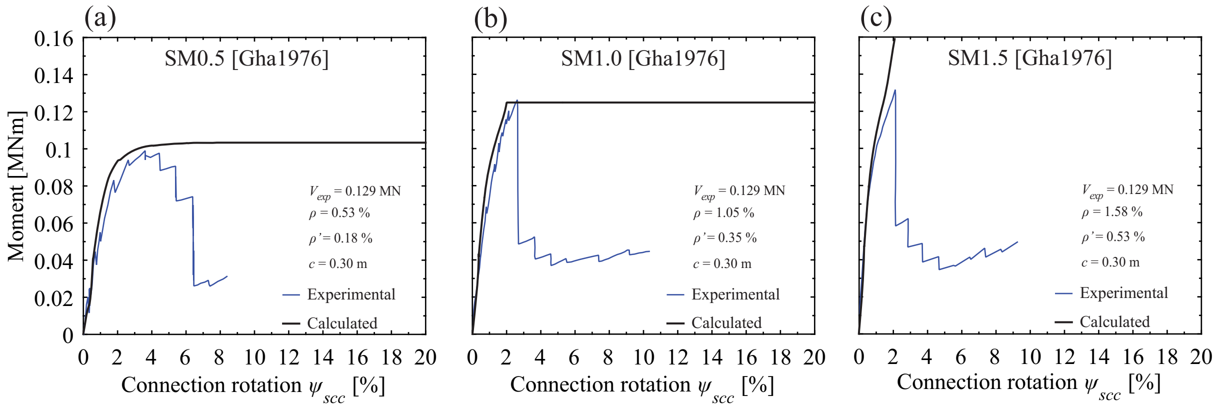

Influence of the flexural reinforcement ratio on the response of slab-column connections

Islam and Park (1976)

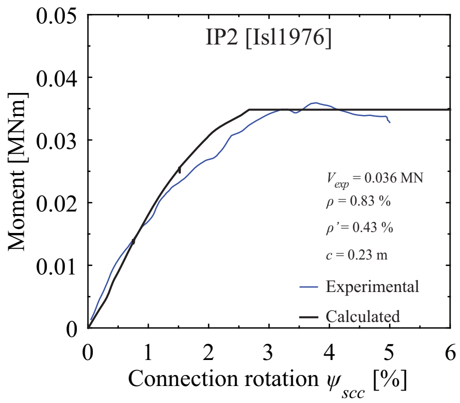

Drakatos et al. (2015)

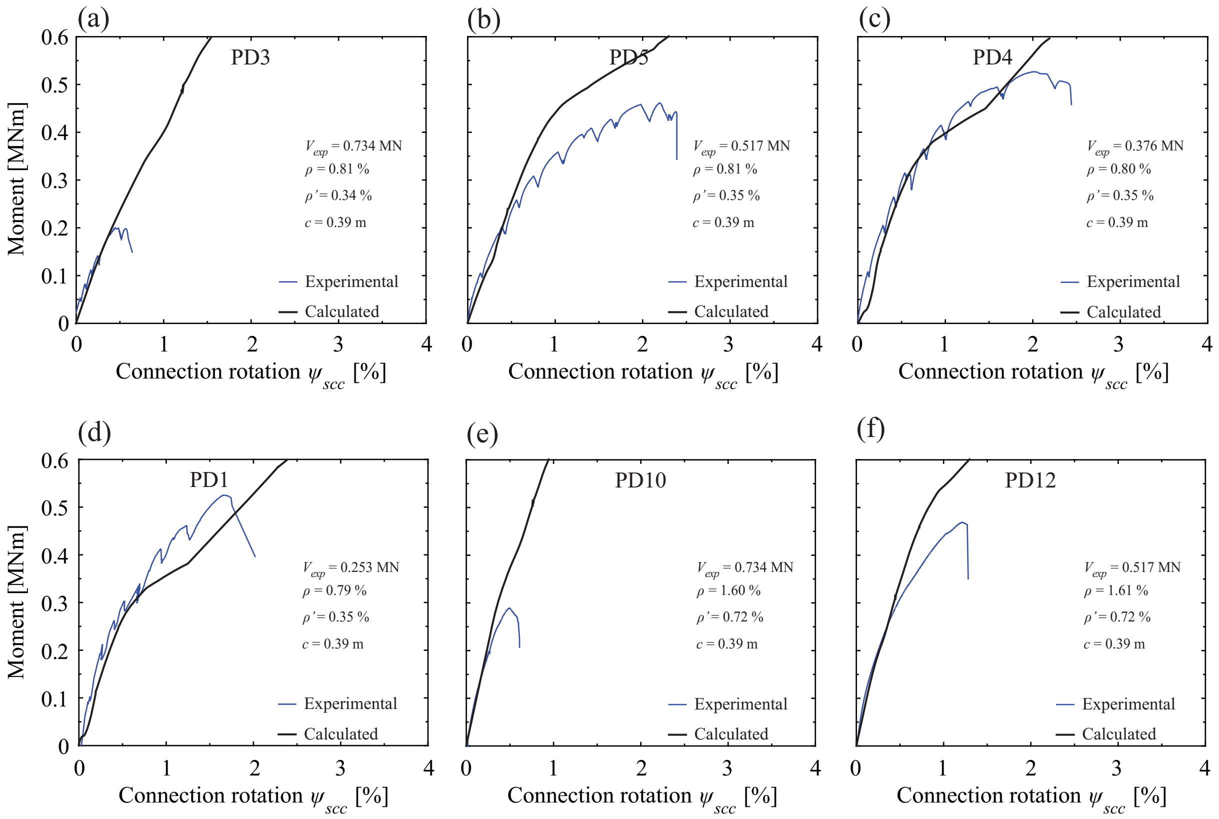

➢ **Constant eccentricity**

Elstner and Hognestad (1956)

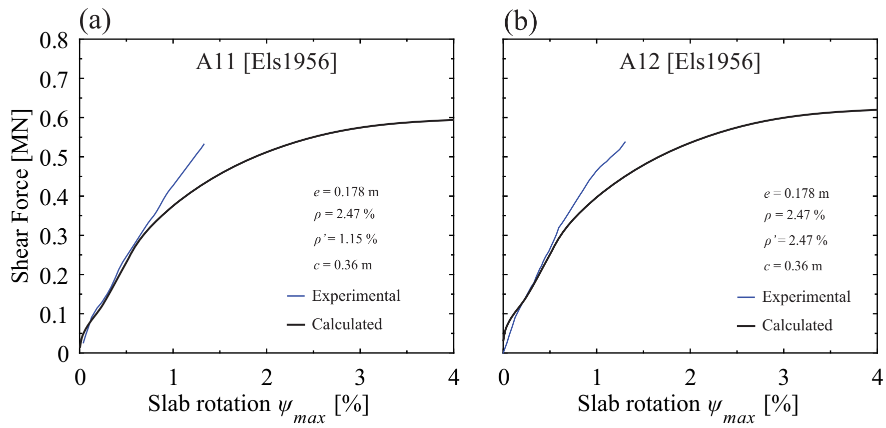

Influence of the bottom reinforcement content on the response of slab-column connections

Hawkins et al. (1989)

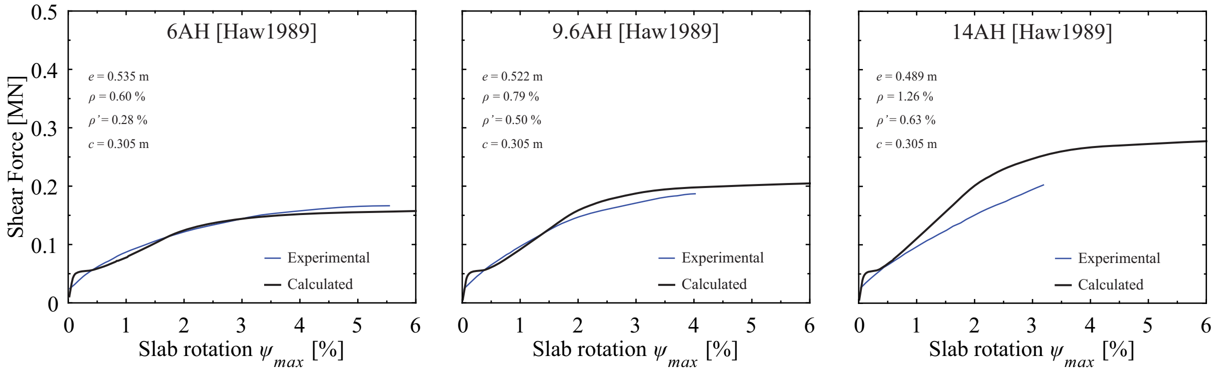

Influence of flexural reinforcement ratio on the response of slab-column connections subjected to high eccentricities

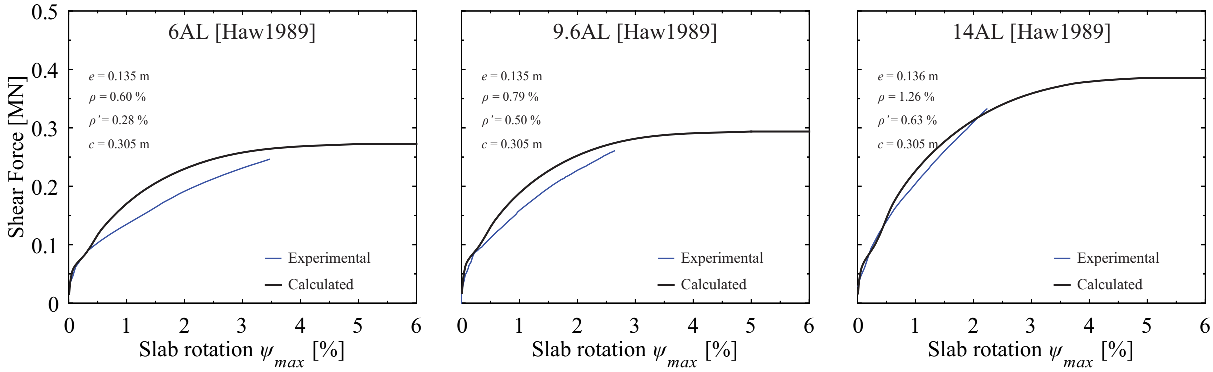

Influence of flexural reinforcement ratio on the response of slab-column connections subjected to low eccentricities

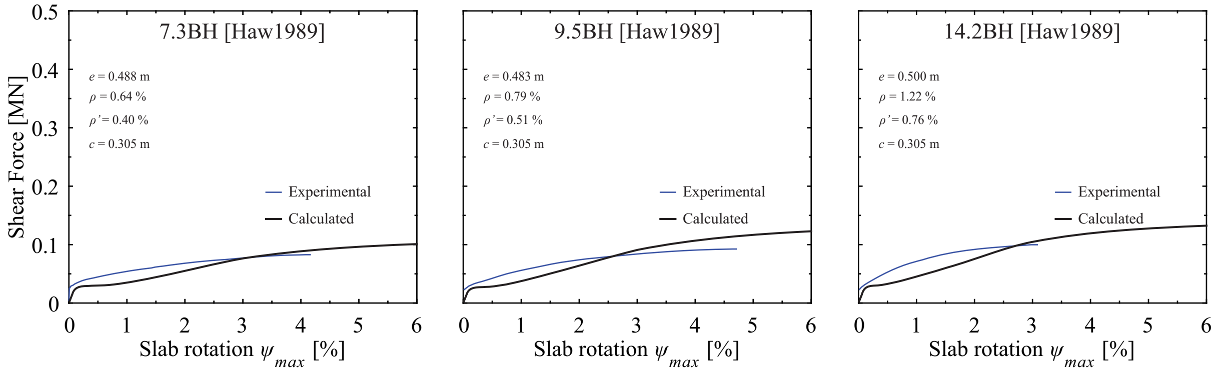

Influence of flexural reinforcement ratio on the response of slab-column connections subjected to high eccentricities (reduced slab thickness)

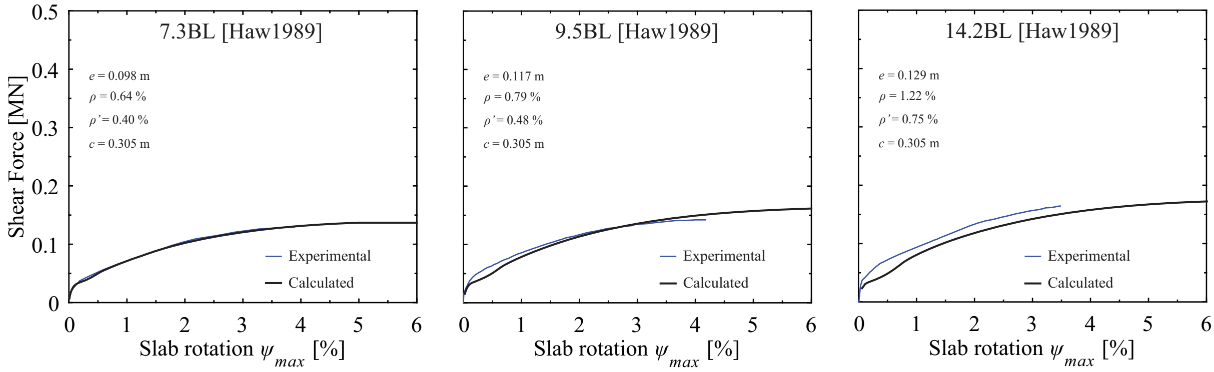

Influence of flexural reinforcement ratio on the response of slab-column connections subjected to low eccentricities (reduced slab thickness)

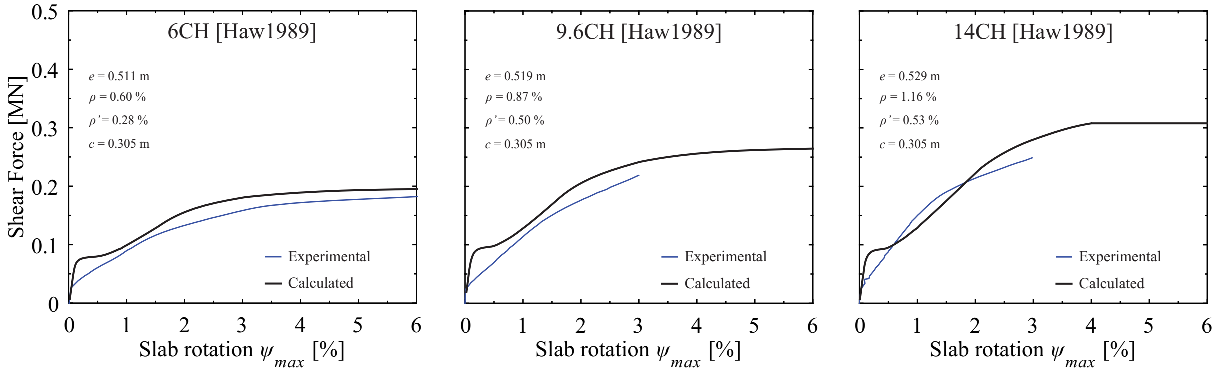

Influence of flexural reinforcement ratio on the response of slab-column connections subjected to high eccentricities (high-strength concrete)

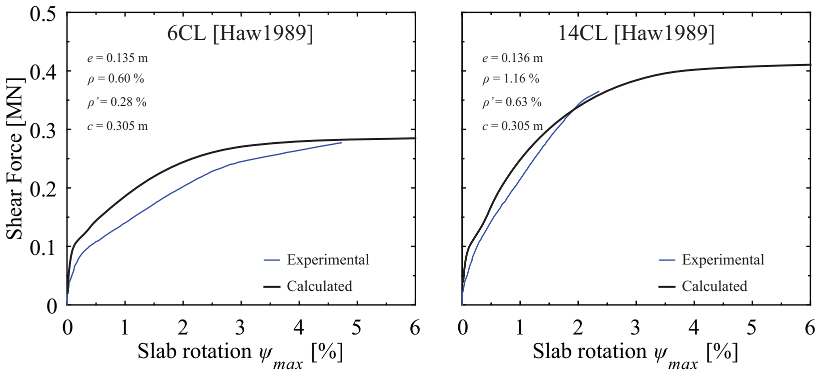

Influence of flexural reinforcement ratio on the response of slab-column connections subjected to low eccentricities (high-strength concrete)

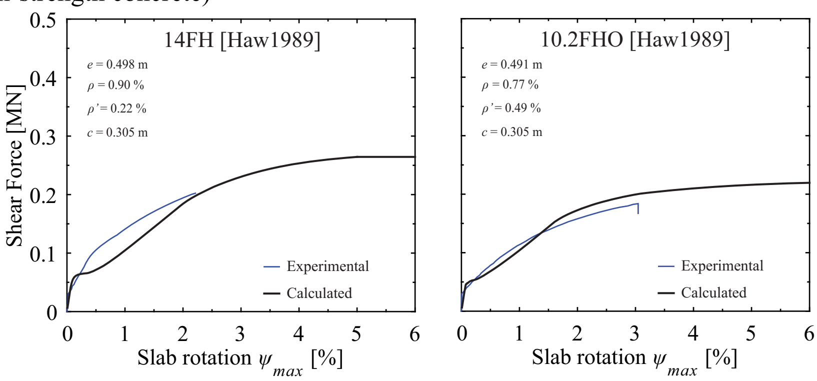

Influence of the flexural reinforcement pattern on the response of slab-column connections subjected to high eccentricities (reduced slab thickness)

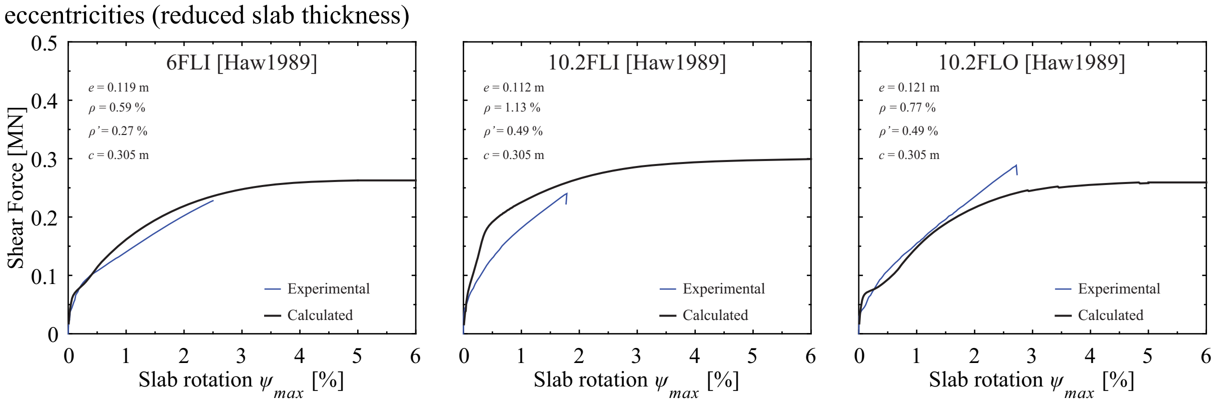

Influence of the flexural reinforcement pattern on the response of slab-column connections subjected to low eccentricities (reduced slab thickness)

Krüger et al. (2000)

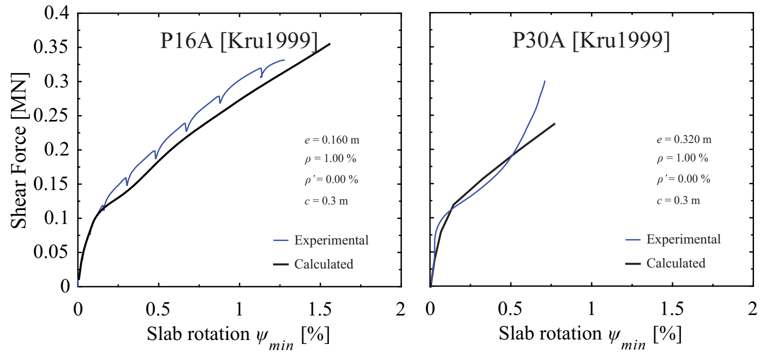

Binici and Bayrak (2005)

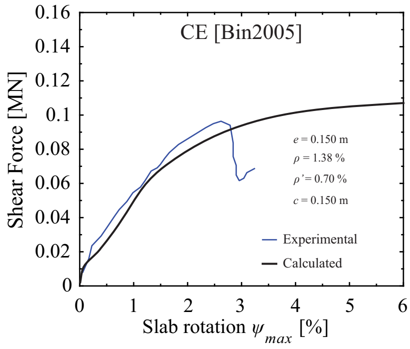

Influence of the level of eccentricity on the response of slab-column connections

- **CYCLIC TESTS**

Kanoh and Yoshizaki (1975)

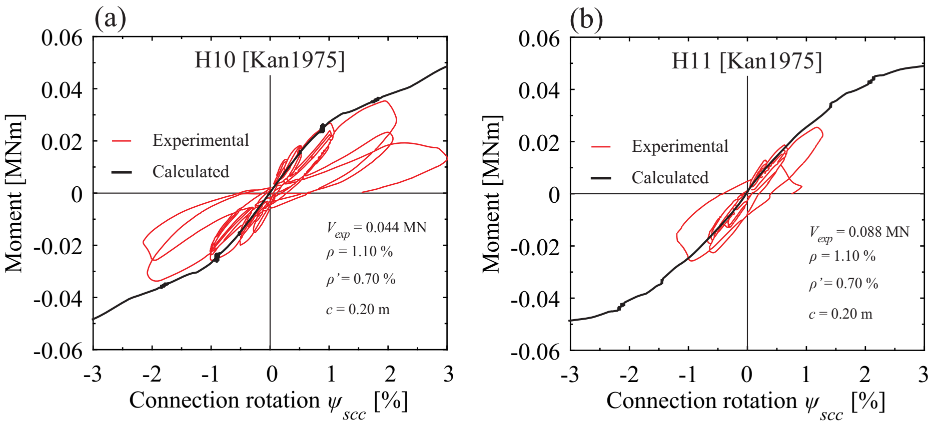

Morrison and Sozen (1983)

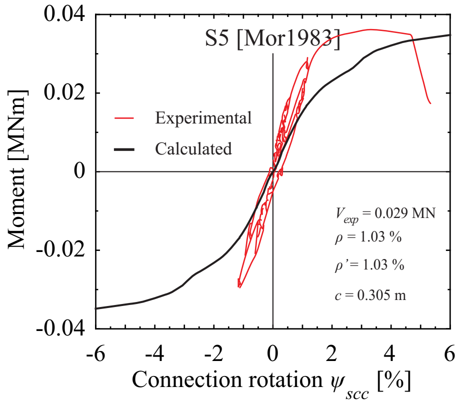

Zee and Moehle. (1984)

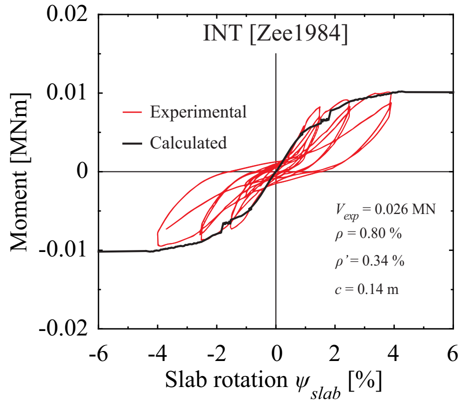

Pan and Moehle (1989)

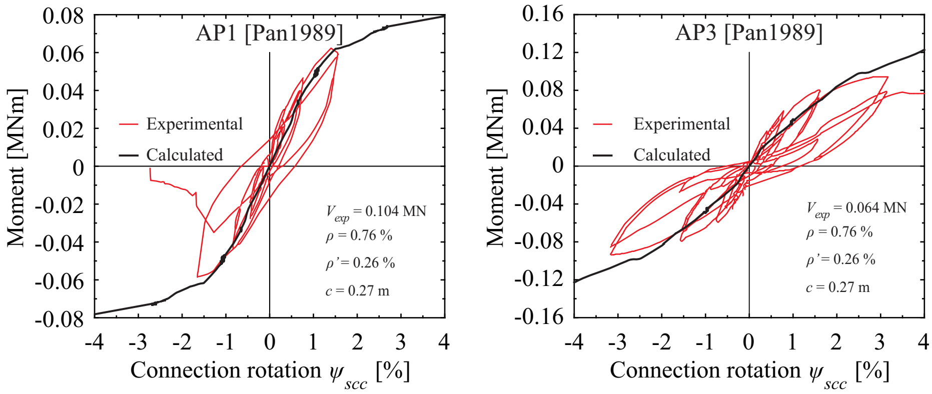

Influence of the vertical load on the response of slab-column connections

Cao (1993)

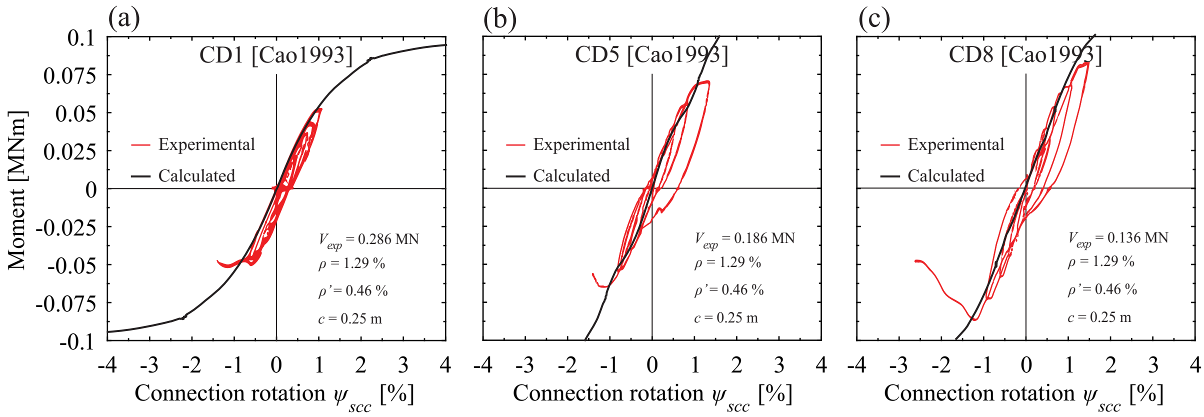

Influence of the vertical load on the response of slab-column connections

Robertson et al. (2002)

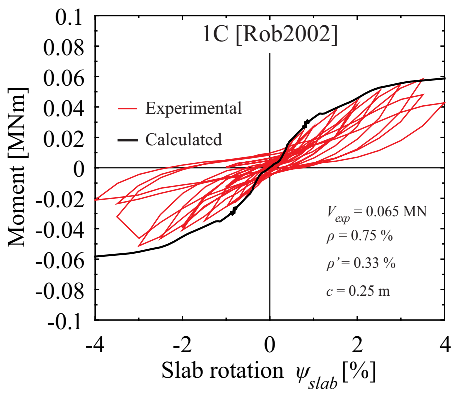

Stark et al. (2005)

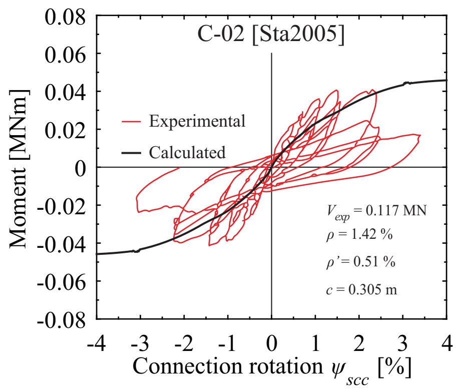

Robertson and Johnson (2006)

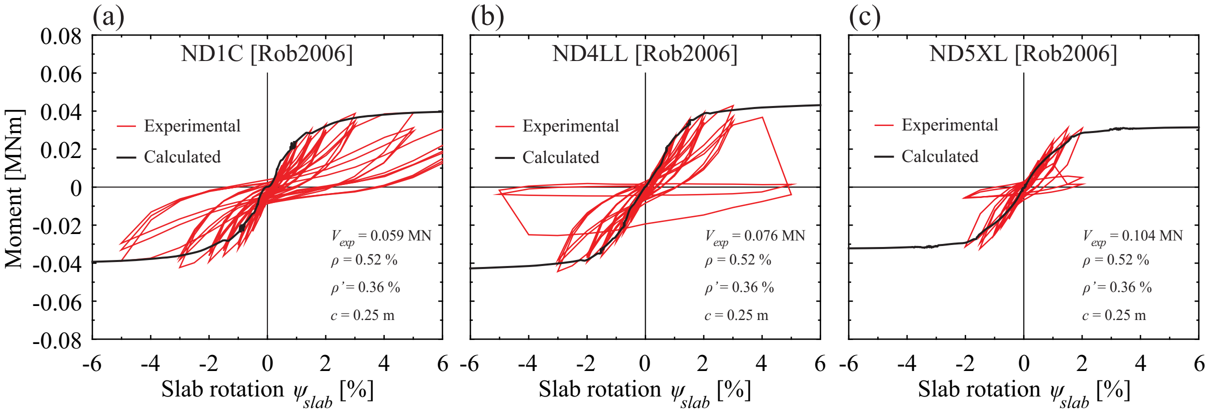

Influence of the vertical load on the response of slab-column connections

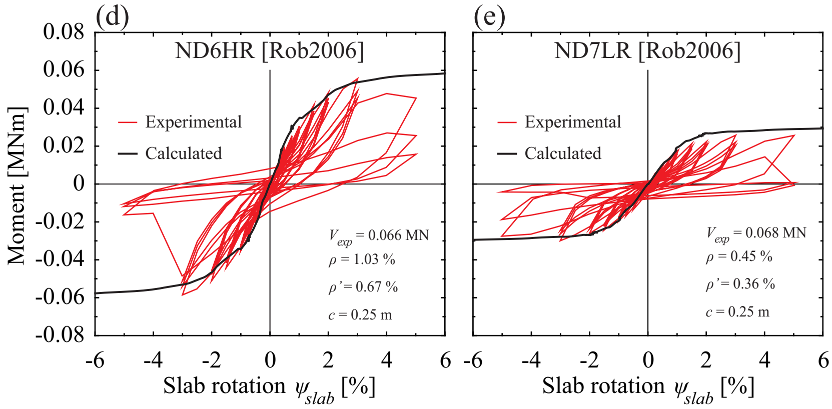

Influence of the flexural reinforcement ratio on the response of slab-column connections

Choi et al. (2007)

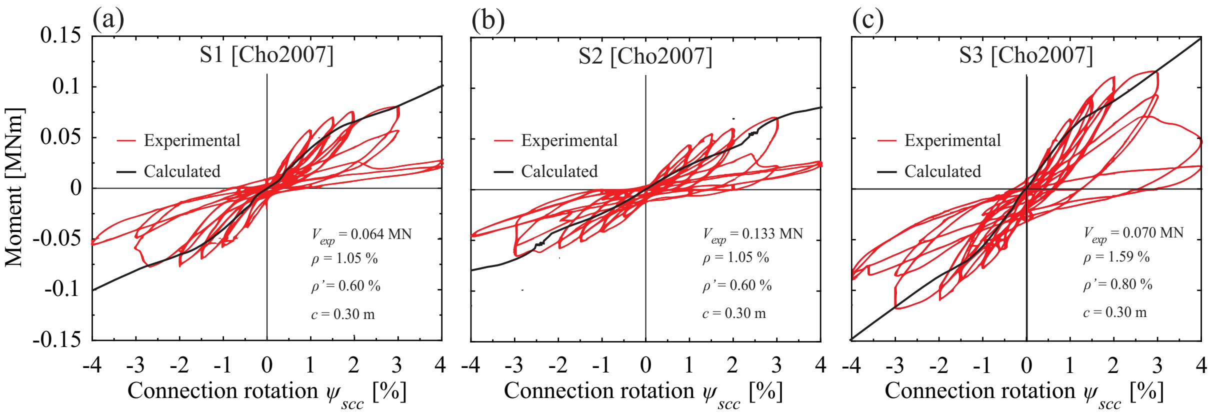

Park et al. (2007)

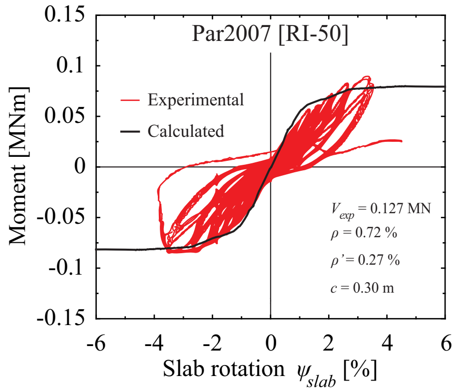

Kang and Wallace (2008)

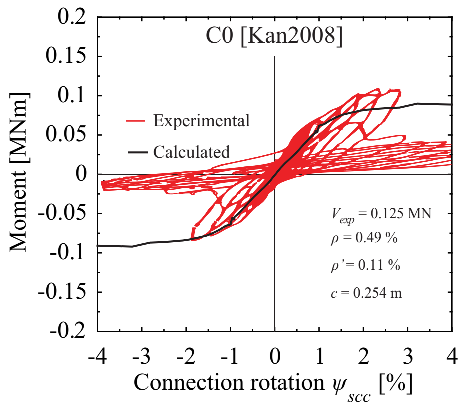

Tian et al. (2008)

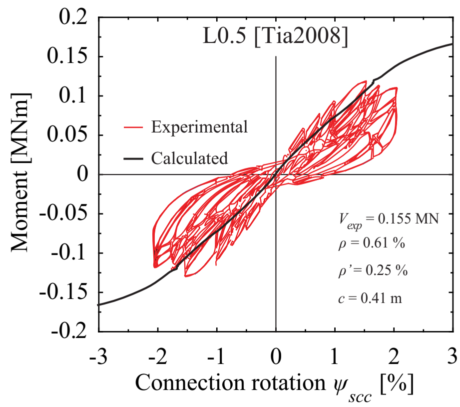

Cho (2009)

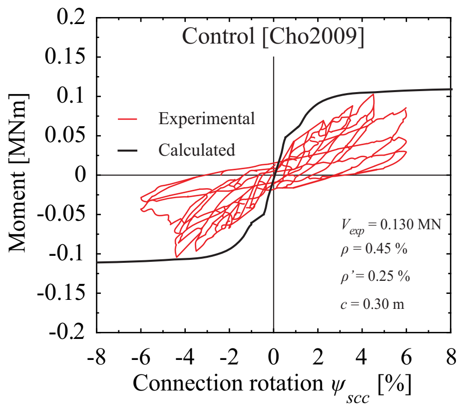

Choi et al. (2009)

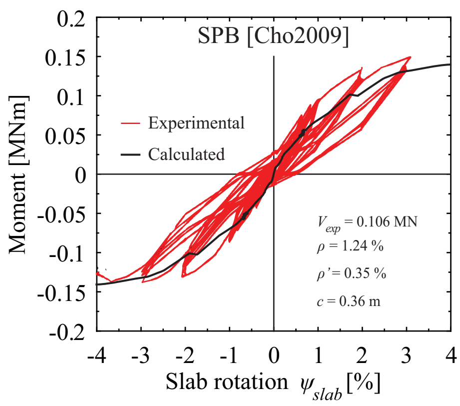

Bu and Polak (2009)

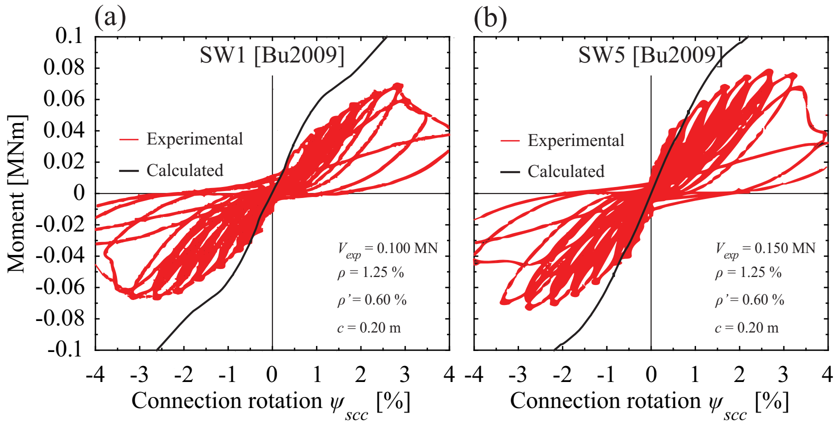

Influence of the vertical load on the response of slab-column connections

Park et al. (2012)

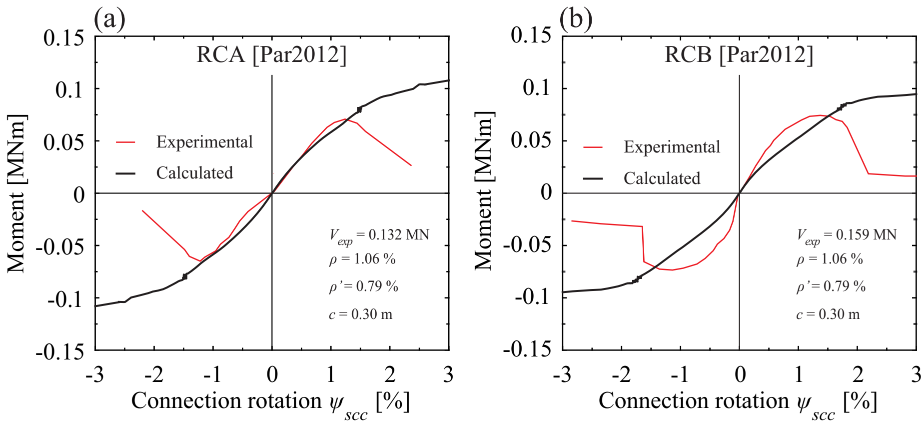

Influence of the vertical load on the response of slab-column connections

Drakatos et al. (2015)

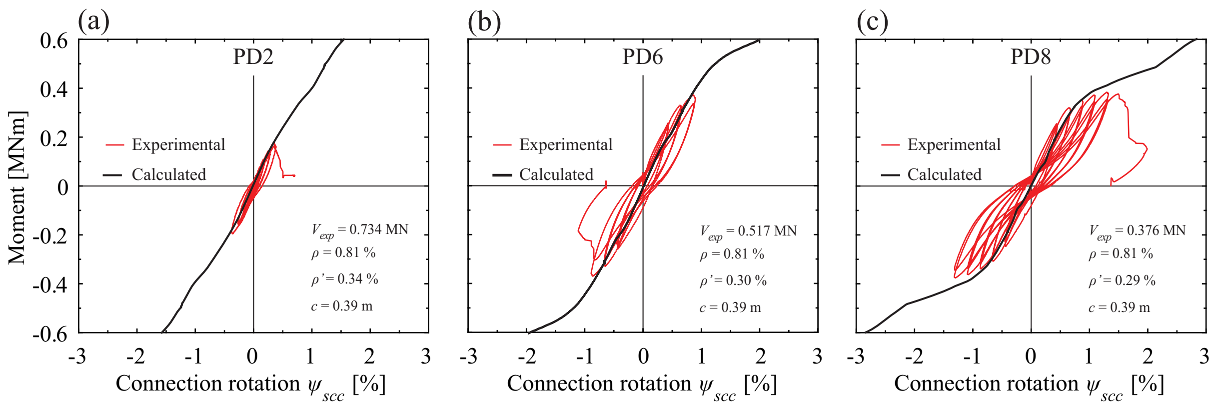

Influence of the vertical load on the response of slab-column connections

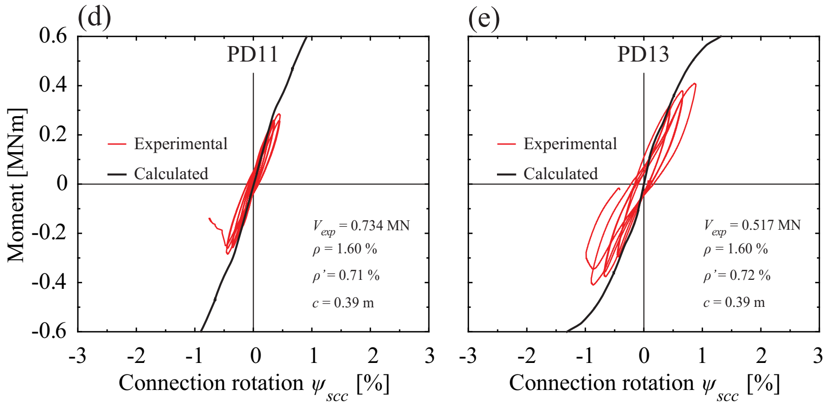

Influence of the vertical load on the response of slab-column connections

APPENDIX IV: Moment and deformation capacity evaluation

Table APP-IV- 1: Strength and deformation capacity predictions for interior slab-column specimens tested under constant vertical load and monotonically increasing moment

Slab	M_{pred} / M_{exp} (-)		$\psi_{scc.pred} / \psi_{scc.exp}$ (-)	
	CSCT (mono)	CSCT (cyc)	CSCT (mono)	CSCT (cyc)
Ghali et al, 1974				
B3NP	0.948	0.695	-	-
B5NP	0.817	0.674	-	-
Stamenkovic and Chapman, 1974				
C/I/1	0.832	0.632	-	-
C/I/2	0.984	0.779	-	-
C/I/3	1.059	0.819	-	-
C/I/4	0.962	0.914	-	-
Ghali et al, 1976				
SM0.5	1.009	0.955	0.928	0.637
SM1.0	0.979	0.880	0.762	0.623
SM1.5	1.268	0.999	1.063	0.760
Islam and Park, 1976				
IP1	1.084	1.084	1.137	1.137
IP2	0.926	0.926	1.094	1.094
Elgabry and Ghali, 1987				
1	1.061	0.822	-	-
Drakatos et al., 2015				
PD1	1.070	0.730	-	-
PD3	1.066	0.945	0.981	0.848
PD4	0.975	0.771	0.876	0.522
PD5	1.021	0.868	0.545	0.390
PD10	1.170	0.881	0.886	0.618
PD12	1.094	0.864	0.721	0.503
Mean (all tests)	**1.018**	**0.847**	**0.899**	**0.713**
Mean (d>0.1m)	**1.040**	**0.840**	**0.845**	**0.613**
COV (all tests)	**0.107**	**0.140**	**0.205**	**0.348**
COV (d>0.1m)	**0.109**	**0.124**	**0.194**	**0.237**

Table APP-IV- 2: Strength and deformation capacity predictions for interior slab-column specimens tested under constant eccentricity and monotonically increasing moment

Slab	M_{pred} / M_{exp} (-)		$\psi_{max.pred}$ / $\psi_{max.exp}$ (-)	
	CSCT (mono)	CSCT (cyc)	CSCT (mono)	CSCT (cyc)
Elstner and Hognestad, 1956				
A11	0.796	0.744	0.906	0.791
A12	0.825	0.768	0.950	0.820
Moe, 1961				
M2	0.927	0.819	-	-
M2A	1.088	0.961	-	-
M3	1.049	0.832	-	-
M4A	1.260	0.966	-	-
M6	0.991	0.892	-	-
M7	0.965	0.930	-	-
M8	1.147	0.937	-	-
M9	1.003	0.945	-	-
M10	1.048	0.893	-	-
Anis, 1970				
B3	0.932	0.880	-	-
B4	1.095	1.008	-	-
B5	1.017	0.861	-	-
B6	0.925	0.759	-	-
B7	1.115	0.876	-	-
Narasimhan, 1971				
L1	0.940	0.841	-	-
Hawkins et al., 1989				
6AH	0.918	0.888	0.915	0.663
9.6AH	1.032	0.958	0.841	0.652
14AH	1.101	0.942	0.762	0.596
6AL	1.058	0.995	0.915	0.724
9.6AL	1.098	1.060	1.133	0.951
14AL	1.002	0.966	0.932	0.851
7.3BH	1.172	1.061	1.115	0.877
9.5BH	1.089	0.929	0.778	0.604
14.2BH	1.096	0.870	1.078	0.755
7.3BL	1.021	0.957	1.028	0.820
9.5BL	1.015	0.934	0.841	0.673
14.2BL	0.868	0.822	0.824	0.729
6CH	1.044	1.024	0.894	0.697
9.6CH	1.157	1.090	1.178	0.916
14CH	1.089	0.949	0.941	0.725
6CL	1.028	1.011	1.044	0.799
14CL	1.036	0.988	1.127	0.966
14FH	1.063	0.919	1.039	0.806
6FLI	1.125	1.091	1.095	0.924
10.2FLI	1.129	1.062	1.082	0.830
10.2FLO	0.863	0.825	1.191	0.928
10.2FHO	1.130	0.987	1.203	0.731
Kamaraldin, 1990				
SA1	0.852	0.808	-	-
SA3	0.987	0.944	-	-
SA4	1.096	0.964	-	-
SB2	1.051	0.883	-	-
Marzouk et al., 2001				
NHLS0.5	0.808	0.791	-	-

Slab	M_{pred} / M_{exp} (-)		$\psi_{max,pred} / \psi_{max,exp}$ (-)	
	CSCT (mono)	CSCT (cyc)	CSCT (mono)	CSCT (cyc)
NHLS1.0	0.886	0.813	-	-
NNHS1.0	1.093	0.893		-
NHHS0.5	0.877	0.831	-	-
NHHS1.0	0.957	0.788	-	-
Krüger et al., 2000				
P16A	0.942	0.898	0.996	0.917
P32	0.976	0.911	0.862	0.820
Binici and Bayrak, 2005				
CE	0.847	0.746	0.924	0.716
Ben-Sasi, 2012				
SI-1	1.077	0.996	-	-
SI-2	0.920	0.835	-	-
Mean (all tests)	**1.012**	**0.912**	**0.985**	**0.788**
Mean (d>0.1m)	**1.013**	**0.920**	**1.000**	**0.805**
COV (all tests)	**0.103**	**0.098**	**0.131**	**0.135**
COV (d>0.1m)	**0.107**	**0.100**	**0.127**	**0.134**

Table APP-IV- 3: Strength and deformation capacity predictions for interior slab-column specimens tested under constant vertical load and cyclically increasing moment

Slab	M_{pred} / M_{exp} (-)		$\psi_{scc,pred}$ / $\psi_{scc,exp}$ (-)	
	CSCT (mono)	CSCT (cyc)	CSCT (mono)	CSCT (cyc)
Kanoh and Yoshizaki, 1975				
H9	1.437	1.094	1.885	1.040
H10	1.457	1.027	1.880	0.970
H11	1.274	1.007	1.386	1.012
Islam and Park, 1976				
IP3C	1.117	1.012	1.393	0.843
Morrison et al., 1983				
S5	0.985	0.924	1.447	0.963
Zee and Moehle, 1984				
INT	0.988	0.954	1.115†	0.964†
Pan and Moehle, 1989				
AP1	1.195	0.986	1.670	0.917
AP3	1.514	1.032	1.596	0.882
Cao, 1993				
CD1	1.164	0.931	1.226	0.897
CD5	1.294	0.992	1.167	0.899
CD8	1.251	0.937	1.469	0.875
Robertson et al., 2002				
1C	1.027	1.011	1.306†	1.208†
Stark et al., 2005				
C-02	0.995	0. 883	1.270	0.988
Robertson and Johnson, 2006				
ND1C	1.000	0.992	1.097†	0.975†
ND4LL	0.968	0.941	1.250†	0.988†
ND5XL	0.944	0.937	1.174†	1.090†
ND6HR	0.989	0.957	1.222†	0.986†
ND7LR	0.928	0.925	1.030†	0.987†
Choi et al., 2007				
S1	1.399	0.998	1.876	1.033
S2	0.993	0.810	0.989	0.809
S3	1.423	0.881	1.878	0.902
Park et al., 2007				
RI-50	0.954	0.949	0.987†	0.937†
Kang and Wallace, 2008				
C0	1.082	1.003	1.739	1.255
Tian et al., 2008				
L0.5	1.225	1.001	1.513	1.121
Bu and Polak, 2009				
SW1	1.320	0.881	-	-
SW5	1.143	0.775	-	-
Cho, 2009				
Control	1.017	1.002	1.133	0.882
Choi et al., 2009				
SPB	1.050	0.988	1.679†	0.930†
Park et al., 2012				
RCA	1.244	0.956	1.382	0.987
RCB	1.216	1.052	1.561	1.190
Drakatos et al., 2015				
PD2	1.153	1.009	1.330	1.132
PD6	1.212	0.971	1.203	0.918
PD8	1.130	0.980	1.169	0.766
PD11	1.233	0.928	1.076	0.721

Slab	M_{pred} / M_{exp} (-)		$\psi_{scc,pred} / \psi_{scc,exp}$ (-)	
	CSCT (mono)	CSCT (cyc)	CSCT (mono)	CSCT (cyc)
PD13	1.269	1.007	1.032	0.718
Mean (all tests)	**1.160**	**0.964**	**1.368**	**0.963**
Mean (d>0.1m)	**1.190**	**0.984**	**1.349**	**0.943**
COV (all tests)	**0.142**	**0.067**	**0.205**	**0.132**
COV (d>0.1m)	**0.105**	**0.036**	**0.169**	**0.174**

†Rotation due to slab deformation ψ_{slab} for tests using setup (c) with the vertical load applied on the slab (To account for simply supported slabs the first term “2” in Eq. 14 is replaced by “3”, the second term “2” and the term “3” are omitted)